A Thermodynamic View of Dusty Protoplanetary Disks

Min-Kai Lin[1,2,3] and Andrew N. Youdin[2]
[1] Institute of Astronomy and Astrophysics, Academia Sinica, Taipei 10617, Taiwan; mklin@asiaa.sinica.edu.tw
[2] Department of Astronomy and Steward Observatory, University of Arizona, Tucson, AZ 85721, USA

Abstract

Small solids embedded in gaseous protoplanetary disks are subject to strong dust–gas friction. Consequently, tightly coupled dust particles almost follow the gas flow. This near conservation of the dust-to-gas ratio along streamlines is analogous to the near conservation of entropy along flows of (dust-free) gas with weak heating and cooling. We develop this thermodynamic analogy into a framework to study dusty gas dynamics in protoplanetary disks. We show that an isothermal dusty gas behaves like an adiabatic pure gas, and that finite dust–gas coupling may be regarded as effective heating/cooling. We exploit this correspondence to deduce that (1) perfectly coupled, thin dust layers cannot cause axisymmetric instabilities; (2) radial dust edges are unstable if the dust is vertically well-mixed; (3) the streaming instability necessarily involves a gas pressure response that lags behind dust density; and (4) dust-loading introduces buoyancy forces that generally stabilize the vertical shear instability associated with global radial temperature gradients. We also discuss dusty analogs of other hydrodynamic processes (e.g., Rossby wave instability, convective overstability, and zombie vortices) and how to simulate dusty protoplanetary disks with minor tweaks to existing codes for pure gas dynamics.

Key words: accretion, accretion disks – hydrodynamics – instabilities – methods: analytical – methods: numerical – protoplanetary disks

1. Introduction

Protoplanetary disks are comprised of a mixture of gas and dust (Chiang & Youdin 2010). Although the overall dust content is small (∼1% by mass), their presence can have profound impacts on the gas dynamics and vice versa. Dust–gas friction introduces phenomena that are absent from pure gas disks. Important examples include the streaming instability (SI, Youdin & Goodman 2005; Johansen & Youdin 2007; Youdin & Johansen 2007), secular gravitational instabilities (SGI, Ward 2000; Youdin 2011; Michikoshi et al. 2012; Takahashi & Inutsuka 2014, 2016; Latter & Rosca 2017) and Kelvin–Helmholtz instabilities (Goldreich & Ward 1973; Chiang 2008; Barranco 2009; Lee et al. 2010).

These instabilities can trigger turbulence, and (in different regimes) promote or inhibit planetesimal formation. More recently, new dusty instabilities have appeared in numerical simulations (Lorén-Aguilar & Bate 2015, 2016; Lambrechts et al. 2016) and analytical calculations (Squire & Hopkins 2017; Hopkins & Squire 2017), but their physical underpinnings are not yet well understood.

Current state-of-the-art models of dusty protoplanetary disks directly simulate gas dynamics coupled to explicit Lagrangian dust particles (Johansen et al. 2006; Nelson & Gressel 2010; Bai & Stone 2010a; Yang & Johansen 2014; Zhu et al. 2014; Gibbons et al. 2015; Baruteau & Zhu 2016; Simon et al. 2016). The equation of motion for each particle is solved including dust–gas drag, the strength of which is measured by a stopping time t_s—the decay timescale for the relative velocity between gas and dust. Thus small t_s corresponds to tightly coupled particles.

Another approach is to model the dust population as a continuous, pressureless fluid (Barrière-Fouchet et al. 2005; Paardekooper & Mellema 2006; Ayliffe et al. 2012; Meheut

et al. 2012; Laibe & Price 2012; Fu et al. 2014; Lorén-Aguilar & Bate 2014; Surville et al. 2016). The hydrodynamic equations are evolved for two fluids: the gas and dust, with density and velocity ρ_g, $\boldsymbol{v}_g$ and ρ_d, $\boldsymbol{v}_d$, respectively. Source terms are introduced into the momentum/energy equations to model dust–gas drag. This approach can take advantage of existing numerical methods/codes for simulating pure gas dynamics. A practical difficulty with this approach is the need to numerically stabilize the pressureless dust fluid with, e.g., artificial diffusion.

The two-fluid equations for dust and gas can be reformulated into equivalent dynamical equations for the center-of-mass velocity $\boldsymbol{v}$ and the relative dust–gas velocity $\boldsymbol{v}_d - \boldsymbol{v}_g$ (Youdin & Goodman 2005). In this reformulation, continuity equations for dust and gas can be replaced by the mass conservation of total density ρ plus the evolution of the dust-to-gas ratio ρ_d/ρ_g (or dust fraction, ρ_d/ρ, Laibe & Price 2014).

This reformulation is particularly advantageous in the tight-coupling limit of $t_s \ll 1/\Omega$, where the orbital frequency Ω sets the characteristic timescale in many disk dynamics problems. Models with two fluids or with Lagrangian solids are numerically difficult to evaluate in this regime, because of stiff drag forces. In the reformulated equations, however, the center-of-mass motion does not experience drag forces and thus is not stiff. Moreover, for $t_s\Omega \ll 1$ the relative motion satisfies the terminal velocity approximation and can be eliminated from the equations. This single-fluid framework for a well-coupled dust–gas mixture facilitates numerical calculations (Price & Laibe 2015), and also simplifies analytic calculations (Youdin & Goodman 2005; Jacquet et al. 2011), which is useful for gaining insight.

In this work, we develop a parallel between this single-fluid description of dust–gas mixtures and standard hydrodynamics. Specifically we recast the evolution of the dust-to-gas ratio as an energy equation for the thermal content of a fluid. This parallel is most precise when the gas in the dust–gas mixture
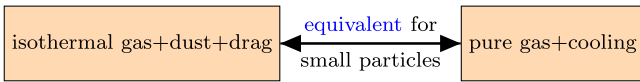
---

[3] Steward Theory Fellow.

Figure 1. The central concept of this work. A mixture of small particles imperfectly coupled to isothermal gas behaves similarly to an adiabatic, pure gas subject to cooling. This permits one to use the equations for standard hydrodynamics to study dust–gas dynamics.

obeys a locally isothermal equation of state for the gas, $P = c_s^2 \rho_g$, where c_s is a prescribed sound-speed profile. This isothermal approximation holds when cooling times are short (Lin & Youdin 2015), e.g., in protoplanetary disks whose temperature is set by external irradiation (Chiang & Goldreich 1997; Stamatellos & Whitworth 2008).

Under these two approximations of strong drag and isothermal gas, we show that the equations of dusty gas dynamics are equivalent to those of nearly adiabatic (i.e., slowly cooling) gas dynamics without dust, see Figure 1. The basis of the analogy is that the entrainment of tightly coupled dust particles in gas flows is similar to the advection of entropy in an adiabatic fluid. Finite dust–gas drag acts as effective heating/cooling: the relative drift between dust and gas causes a fluid parcel to exchange dust particles with its surroundings—an effect similar to heat exchange between a gas parcel and its surroundings. Needless to say, the effective heating term must have a specific form, which we derive, for the equivalence to hold.

The purpose of our physical and mathematical parallel between dusty gas and standard hydrodynamics is to gain a deeper understanding of the dynamics and stability of dusty protoplanetary disks. We can apply established methods to generalize previous stability results for pure gas dynamics to dusty disks. We show that strictly isothermal disks with perfectly coupled dust are generally stable to axisymmetric perturbations, unless the dust-to-gas ratio varies more rapidly in radius than in height. We put forward a thermodynamical interpretation of dust–gas drag instabilities, and apply it to the SI. We also study the effect of dust-loading on the vertical shear instability (VSI) previously considered in pure gas disks (Nelson et al. 2013; Lin & Youdin 2015; Barker & Latter 2015).

This paper is organized as follows. In Section 2 we describe a key insight of our study, that pressure work (i.e., "PdV") can explain the basis of several instabilities, including SI and VSI, in terms of pressure–density phase lags. This motivates us to seek an analogy between dust–gas mixtures and pure gas. We develop our formalism in Section 3 by transforming the two-fluid equations of a tightly coupled dusty gas into single-fluid hydrodynamic equations with a special cooling function. Here we also define the effective entropy and buoyancy of our model fluid. In Section 4 we discuss general stability properties of dusty disks. We then analyze explicit disk models in Section 5, where we show that radial dust edges are unstable, and revisit the SGI and SI in the tight-coupling regime. In Section 6 we extend the VSI to dusty disks. We discuss future applications of the dusty/adiabatic gas equivalence in Section 7 before summarizing in Section 8.

2. Growing Oscillations by Doing Work

In this section we provide physical arguments to highlight the similarity between single-phase fluids and dust–gas mixtures. The mathematical description of this section is deferred to Section 4.4.
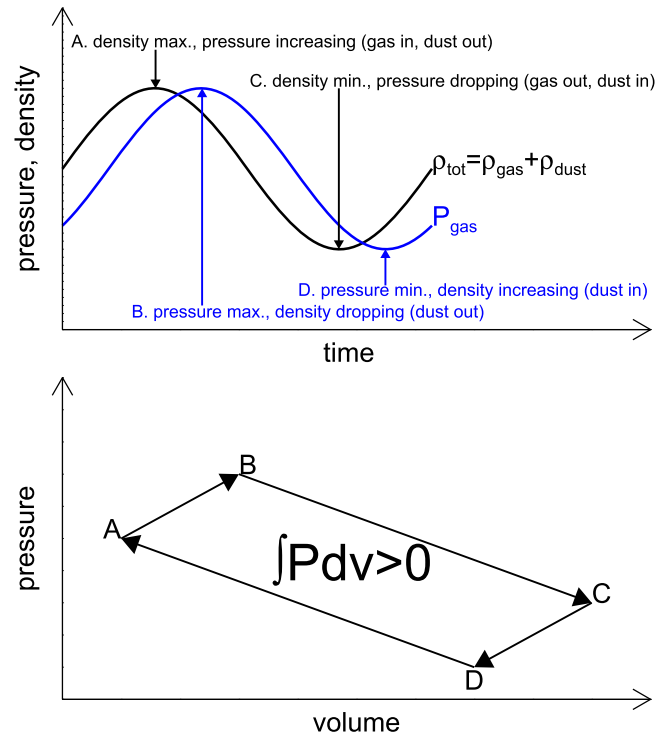

Figure 2. Thermodynamic interpretation of growing oscillations in a fluid. Top: evolution of pressure and density in time. Bottom: oscillation cycle in the P–V plane. In the case shown, dust drag causes pressure (due to gas only) to lag behind total density. This results in a clockwise path in the P–V plane, implying positive work done by the fluid, which would increase oscillation amplitudes.

It is well known that in the limit of perfect coupling the addition of dust increases the gas inertia but not pressure. One can then regard dusty gas as a single fluid with a reduced sound speed. Here, we argue that when dust–gas coupling is imperfect, there exists another similarity with pure gas, related to the phase of pressure and density evolution. Thus it is still possible to regard partially coupled dusty gas as a single fluid.

A general result in fluid dynamics is that work is done whenever oscillations in the pressure and density of the fluid are not in phase. If the average work done is positive, then oscillation amplitudes grow: the work done allows the system to "overshoot" beyond the amplitude of preceding oscillations.

Figure 2 gives a graphical demonstration that if pressure lags behind density, then positive is work done because it leads to a clockwise path in the "P–V" plane. The annotations consider the particular case where the phase lag arises because the fluid has two components (gas and dust, see below) but the following description is general.

From A to B, a fluid parcel is expanding to return to equilibrium, but pressure is still increasing. This overcompensation will cause the parcel to expand beyond the maximum volume of the previous cycle. Similarly, from C to D the parcel is already contracting toward equilibrium, but pressure is still dropping. This allows the parcel's contraction to overshoot the maximum density attained in the previous cycle. The overall positive work done leads to growth in the oscillation amplitude. This effect is similar to being pushed downward on a swing when descending.

There are several situations where the pressure and density of a fluid are not in phase. The obvious case is if the fluid is subject to external heating/cooling. For example, in strongly irradiated protoplanetary disks the disk temperature $T(r)$ is

time-independent but varies with the cylindrical radius r from the star (Chiang & Goldreich 1997). Since $P \propto \rho_g T$ for an ideal gas, there is no reason to expect P and ρ_g to be in phase as a gas parcel oscillates between different radii and adopts the corresponding local temperatures. In fact, we will show that this is a fundamental property of the VSI (Lin & Youdin 2015).

Another possibility, as annotated in Figure 2, is a dusty gas. The relevant density here is the total density $\rho = \rho_d + \rho_g$, but the fluid pressure P is due to gas only. If dust were perfectly coupled to the gas, then P and ρ would be in phase, and there is no work done. However, for finite dust–gas drag, ρ_d and ρ_g are not necessarily in phase, because dust particles can drift relative to the gas, i.e., the dust-to-gas ratio evolves in time. If this causes P to lag ρ, then the positive work done would lead to growing oscillations. Indeed, we show that this is true for the SI.

In order to apply this thermodynamic interpretation of dust–gas drag instabilities, we need to develop a formal analogy between dusty gas and pure hydrodynamics. We show this is possible in the limit of strong drag and a fixed equation of state for the gas.

3. Single-fluid Description of Dusty Gas

We model an accretion disk as a mixture of gas with dust treated as a pressureless fluid. We denote their density and velocity field as (ρ_g, v_g) and (ρ_d, v_d), respectively. The mixture has total density

$$\rho \equiv \rho_g + \rho_d, \qquad (1)$$

and center-of-mass velocity

$$v \equiv \frac{\rho_g v_g + \rho_d v_d}{\rho}, \qquad (2)$$

a single temperature T, and its pressure P arises solely from the gas component. Our goal is to obtain a set of equations describing the dust–gas mixture that resembles standard, single-phase hydrodynamics.

The dust and gas fluids interact via a drag force parameterized by the relative stopping time t_s such that

$$\rho_d \frac{\partial v_d}{\partial t}\bigg|_{\mathrm{drag}} = -\rho_g \frac{\partial v_g}{\partial t}\bigg|_{\mathrm{drag}} = -\frac{\rho_g \rho_d}{\rho} \frac{(v_d - v_g)}{t_s} \qquad (3)$$

is the dust–gas friction force per unit volume. Note that t_s differs slightly from the *particle* stopping time $\tau_s = t_s \rho/\rho_g$ used in some studies (e.g., Youdin & Goodman 2005).

In general the relative velocity $v_d - v_g$ obeys a complicated evolutionary equation (see, e.g., Youdin & Goodman 2005). However, for tightly coupled dust particles with $t_s \Omega_K \ll 1$, where Ω_K is the Keplerian orbital frequency (since we are interested in protoplanetary disks), we can use the "terminal velocity approximation" to set

$$v_d - v_g = \frac{\nabla P}{\rho_g} t_s \qquad (4)$$

(Jacquet et al. 2011). This equation reflects the well-known effect of particle drift toward pressure maximum (Weidenschilling 1977).

Under the terminal velocity approximation the dust–gas mixture obeys the first-order (in t_s) one-fluid equations:

$$\frac{D\rho}{Dt} = -\rho \nabla \cdot v, \qquad (5)$$

$$\frac{Df_d}{Dt} = -\frac{1}{\rho} \nabla \cdot (f_d t_s \nabla P), \qquad (6)$$

$$\frac{Dv}{Dt} = -\nabla \Phi_{\mathrm{tot}} - \frac{1}{\rho} \nabla P, \qquad (7)$$

$$\frac{DT}{Dt} = -(\gamma - 1) T \nabla \cdot v + \mathcal{H} + \mathcal{H}_{\mathrm{eff}} - \Lambda \qquad (8)$$

(see Laibe & Price 2014; Price & Laibe 2015 for a detailed derivation from the two-fluid equations), where $D/Dt \equiv \partial_t + v \cdot \nabla$ is the Lagrangian derivative *following the mixture*'s center-of-mass velocity v. For an ideal gas the pressure is given by $P = \mathcal{R} \rho_g T/\mu$, where $\mathcal{R}$ is the gas constant and μ is the mean molecular weight.

Equation (6) is obtained from the dust continuity equation, $\partial_t \rho_d + \nabla \cdot (\rho_d v_d) = 0$, by writing $v_d = v + t_s \nabla P/\rho$ and eliminating ρ_d in favor of the dust fraction f_d:

$$f_d \equiv \frac{\rho_d}{\rho} = \frac{\epsilon}{1 + \epsilon}, \qquad (9)$$

where $\epsilon = \rho_d/\rho_g$ is the usual dust-to-gas ratio. If $t_s = 0$ then the dust-to-gas ratio is conserved following the fluid. Otherwise, ϵ evolves due to particle drift in response to pressure gradients. Note that Equation (6) is equivalent to Equation (46) of Jacquet et al. (2011).

The total gravitational potential $\Phi_{\mathrm{tot}} = \Phi + \psi$ includes that from a central star of mass M_* and the disk's own potential ψ. We adopt

$$\Phi(r, z) = -\frac{GM_*}{\sqrt{r^2 + z^2}} \simeq -\frac{GM_*}{r}\left(1 - \frac{z^2}{2r^2}\right), \qquad (10)$$

where (r, ϕ, z) are cylindrical coordinates centered on the star and G is the gravitational constant. The second equality is the thin-disk approximation, appropriate for $|z| \ll r$. We use this approximate form in order to obtain explicit expressions for disk equilibria (Section 5.1). The disk potential ψ satisfies the Poisson equation

$$\nabla^2 \psi = 4\pi G \rho. \qquad (11)$$

We include ψ for completeness, but we will mostly neglect it unless stated otherwise.

For the mixture's temperature evolution, Equation (8), γ is the adiabatic index of the gas; $\mathcal{H}$ represents heating and $\mathcal{H}_{\mathrm{eff}}$ is an effective source term arising from transforming the gas energy equation (Equation (17)) from the two-fluid to one-fluid variables (see Laibe & Price 2014 for details). We also include a simple model of radiative cooling,

$$\Lambda = \frac{T - T_{\mathrm{ref}}}{t_{\mathrm{cool}}}, \qquad (12)$$

which relaxes the mixture back to a prescribed temperature profile T_{ref} on a timescale of t_{cool}. We will shortly simplify the problem by considering rapid cooling, $t_{\mathrm{cool}} \to 0$.

Equations (5)–(8) are not yet equivalent to standard hydrodynamics, which typically evolves two scalar fields—

the density and temperature (or pressure). By contrast, Equations (5)–(8) involve three scalars: ρ, f_d, and T. However, we can establish an analogy by fixing the equation of state for the gas, thus eliminating Equation (8), but then reformulating the evolution of the dust-to-gas ratio, Equation (6), into an energy-like equation.

3.1. Locally Isothermal Equation of State

We consider the limit of short cooling times, $t_{cool} \rightarrow 0$, appropriate for the outer parts of an irradiated protoplanetary disk (Chiang & Goldreich 1997; Lin & Youdin 2015). Then the disk temperature $T = T_{ref}$ at all times, and so we may adopt a locally isothermal equation of state

$$P = c_s^2(r, z)\rho_g = c_s^2(1 - f_d)\rho, \qquad (13)$$

where $c_s(r, z) = \sqrt{\mathcal{R}T_{ref}/\mu}$ is a prescribed sound-speed profile fixed in time. In most applications we consider vertically isothermal disks with

$$c_s^2(r) \propto r^q, \qquad (14)$$

where q is the power-law index for the disk temperature. For $q = 0$ the disk is strictly isothermal.

Notice that Equation (13) resembles an ideal-gas equation of state but with a reduced temperature $\tilde{T} = T_{ref}(1 - f_d)$. This reduced temperature decreases with dust-loading. Since f_d typically decreases away from the midplane, we expect vertically isothermal dusty disks to behave as if the temperature *increased* away from $z = 0$.

3.2. Effective Energy Equation

Although we have deleted the true energy equation by fixing a locally isothermal equation of state, we show that the mixture nevertheless obeys an effective energy evolution equation. This is because advection of the dust fraction, described by Equation (6), can be transformed into an energy-like equation. The equation of state, Equation (13), implies

$$f_d = 1 - \frac{P}{c_s^2(r, z)\rho}.$$

Then Equation (6) becomes

$$\frac{\partial P}{\partial t} + \boldsymbol{v} \cdot \nabla P = -P\nabla \cdot \boldsymbol{v} + P\boldsymbol{v} \cdot \nabla \ln c_s^2 + \mathcal{C}, \qquad (15)$$

$$\mathcal{C} \equiv c_s^2 \nabla \cdot \left[t_s \left(1 - \frac{P}{c_s^2 \rho} \right) \nabla P \right]. \qquad (16)$$

For comparison with the standard energy equation in hydrodynamics, rewriting Equation (8) for a pure ideal gas with $P \propto \rho_g T$, and reverting back to gas velocities, gives

$$\frac{\partial P}{\partial t} + \boldsymbol{v}_g \cdot \nabla P = -\gamma P\nabla \cdot \boldsymbol{v}_g + \frac{P}{T}(\mathcal{H} - \Lambda). \qquad (17)$$

We can thus interpret Equation (15) as the energy equation for an ideal gas with adiabatic index $\gamma = 1$, but now with the imposed temperature gradient ∇c_s^2 and dust–gas drag $\mathcal{C}$ acting as source terms.

If we denote the pressure forces by

$$\boldsymbol{F} \equiv -\frac{\nabla P}{\rho}, \qquad (18)$$

then

$$\mathcal{C} = -c_s^2 \nabla (f_d t_s \rho \boldsymbol{F}),$$

which is in the same form as cooling by radiative diffusion. In protoplanetary disks the corresponding "heat flux," proportional to $\boldsymbol{F}$, is directly radially outward and vertically upward. This is simply a reflection of particle drift toward increasing pressure (inward and downward). Particle flux into a region contributes to "cooling" of that region because the reduced temperature is lowered.

3.3. Entropy and Buoyancy of Isothermal Dusty Gas

The specific entropy of an ideal gas is $S = C_P \ln(P^{1/\gamma}/\rho_g)$, where C_P is the heat capacity at constant pressure.

Since we have shown that a locally isothermal dusty gas effectively has $\gamma = 1$ we can define an effective entropy for the *mixture* as

$$S_{eff} \equiv \ln\frac{P}{\rho} = \ln[c_s^2(1 - f_d)], \qquad (19)$$

where the constant heat capacity has been absorbed into S_{eff}. Then combining Equations (15) and (5) gives

$$\frac{DS_{eff}}{Dt} = \boldsymbol{v} \cdot \nabla \ln c_s^2 + \frac{c_s^2}{P}\nabla \cdot (t_s f_d \nabla P),$$

which is equivalent to entropy evolution in standard hydrodynamics, albeit with source terms. With an effective entropy defined this way, many of the results concerning the stability of (locally) isothermal dusty gas will have identical form and interpretations to those for pure gas.

The physical reason for this analogy is that with strong drag ($t_s \rightarrow 0$), dust is almost perfectly entrained in the gas, but there is some gain/loss of dust particles between different gas parcels. This is analogous to the entropy of an ideal pure gas subject to heating/cooling: entropy is conserved following a gas parcel, except if there is heat exchange between a fluid parcel and its surroundings. For strictly isothermal gas perfectly coupled to dust (constant c_s^2 and $t_s = 0$) we have $DS_{eff}/Dt = Df_d/Dt = 0$. In this case the effective entropy is exactly conserved because the dust fraction is "frozen in" the flow.

We can now define the vertical buoyancy frequency N_z of the mixture as

$$N_z^2 \equiv -\frac{1}{\rho}\frac{\partial P}{\partial z}\frac{\partial S_{eff}}{\partial z} = c_s^2(r)\frac{\partial \ln \rho_g}{\partial z}\frac{\partial f_d}{\partial z}, \qquad (20)$$

where the second equality assumes a vertically isothermal disk. Protoplanetary disks have $\partial_z \rho_g < 0$, thus stability against vertical convection ($N_z^2 > 0$) requires $\partial_z f_d < 0$, i.e., the dust density should drop faster than the gas density away from the midplane. This is equivalent to entropy increasing away from the midplane. A similar expression exists for the radial buoyancy frequency N_r, but $|N_r| \ll |N_z|$ in thin, smooth disks.

A vertical buoyancy force exists even in vertically isothermal dusty disks, because coupling gas to dust particles

increases the fluid's inertia, but pressure (i.e., restoring) forces are unchanged. The increased weight of the fluid resists vertical oscillations and hence there is an associated buoyancy force. However, if $t_s \neq 0$ so the gas–dust coupling is imperfect, then gas is no longer "weighed down" by the dust and can slip past it. Thus finite drag diminishes the dust-induced buoyancy. This is similar to reducing gas buoyancy through cooling (Lin & Youdin 2015).

3.4. Physical Disk Conditions

The above correspondence between isothermal dusty gas and adiabatic pure gas is derived under the terminal velocity approximation, which applies to short stopping times, $t_s\Omega_K \ll 1$, and the locally isothermal approximation, which applies to short cooling times, $t_{cool}\Omega_K \ll 1$. In typical protoplanetary disk models such as the Minimum Mass Solar Nebula, t_s decreases for smaller particles and/or toward smaller radii (Youdin 2011). However, t_{cool} is generally small only in the outer disk (Lin & Youdin 2015; Malygin et al. 2017). Combining these results, we estimate that the correspondence will be applicable to particles of less than millimeter size at a few to tens of au in protoplanetary disks. However, note that the isothermal approximation may be relaxed to other fixed equations of state (see Section 7.2).

4. General Stability Criteria for Dusty Gas

In this section we discuss the stability properties of the dusty gas mixture using a variational principle. This approach does not require explicit solutions (i.e., a specific distribution of the density and dust-to-gas ratio) to the equilibrium equations. We consider axisymmetric systems and neglect self-gravity here.

4.1. Steady States

For a given distribution of the dust fraction f_d (or dust-to-gas ratio ϵ), the mass and momentum Equations (5)–(7) admit solutions with $\rho(r, z)$ and $\mathbf{v} = r\Omega(r, z)\hat{\boldsymbol{\phi}}$ where $\Omega = v_\phi/r$, which satisfy

$$r\Omega^2 = \frac{\partial\Phi}{\partial r} + \frac{1}{\rho}\frac{\partial P}{\partial r}, \qquad (21)$$

$$0 = \frac{\partial\Phi}{\partial z} + \frac{1}{\rho}\frac{\partial P}{\partial z}, \qquad (22)$$

with $P = P(f_d, \rho)$ given by the equation of state (Equation (13)). An explicit solution is presented in Section 5.1, when we analyze the stability of protoplanetary disks.

The mixture possesses vertical shear. To see this, we eliminate Φ between Equations (21) and (22) to obtain

$$r\frac{\partial\Omega^2}{\partial z} = \frac{1}{\rho}\left(\frac{\partial P}{\partial r}\frac{\partial S_{eff}}{\partial z} - \frac{\partial P}{\partial z}\frac{\partial S_{eff}}{\partial r}\right). \qquad (23)$$

and recall that $S_{eff} = \ln[c_s^2(1 - f_d)]$. It is well appreciated that vertical stratification of the dust layer contributes to vertical shear (Chiang 2008). Equation (23) shows that a radial dust stratification ($\partial_r f_d$) also contributes to vertical shear.

Our equilibrium solutions satisfy the hydrostatic constraints of Equations (21)–(22) but are not in general steady-state solutions to the energy Equation (15), because the source term $\mathcal{C} \neq 0$ for realistic disks. Limiting cases with $\mathcal{C} \equiv 0$ include (1)

unstratified or 2D, razor-thin disk models with finite dust–gas drag; (2) perfectly coupled dust with $t_s = 0$. The following analyses thus apply strictly to these limiting cases of $\mathcal{C} = 0$ in equilibrium. Our analysis is also a good approximation when t_s is sufficiently small such that the evolution of the background disk (e.g., dust settling) occurs on much longer timescales than the instability growth timescales.

4.2. Integral Relation

We consider axisymmetric Eulerian perturbations to a variable X of the form

$$\mathrm{Re}\,[\delta X(r, z)\exp(-i\sigma t)], \qquad (24)$$

where σ is the complex mode frequency. We write

$$\sigma = is - \omega, \qquad (25)$$

where s and ω are the growth rate and real frequencies, respectively. Then perturbations have time dependence $e^{st+i\omega t}$. Thus for $\omega > 0$, perturbations rotate anticlockwise in the complex plane.

In Appendix A we linearize Equations (5), (7), and (15) to derive the following integral relation:

$$\sigma^2\mathcal{I}^2 = \int \left[\rho|\delta v_r|^2 A + \rho(\delta v_z\delta v_r^* + \delta v_z^*\delta v_r)B + \rho|\delta v_z|^2 D \right.$$
$$\left. + \frac{1}{P}|\nabla\cdot(P\delta\mathbf{v})|^2\right]dV - \int(\nabla\cdot\delta\mathbf{v}^*)\delta\mathcal{C}dV$$
$$- \int P(\nabla\cdot\delta\mathbf{v}^*)(\delta\mathbf{v}\cdot\nabla\ln c_s^2)dV, \qquad (26)$$

where * denotes the complex conjugate,

$$\mathcal{I}^2 \equiv \int\rho(|\delta v_r|^2 + |\delta v_z|^2)dV \qquad (27)$$

is the meridional kinetic energy, and coefficients A, B, D can be read off Equation (77). We now consider various limits of Equation (26).

4.3. Strictly Isothermal Gas Perfectly Coupled to Dust

When c_s^2 is a constant and $t_s = 0$ (so that $\mathcal{C} = 0$), the dusty gas equations are exactly equivalent to those for adiabatic hydrodynamics with unit adiabatic index. Although the gas is strictly isothermal, the mixture behaves adiabatically because the dust fraction f_d is advected with the gas. This is similar to entropy conservation following an adiabatic gas without heating or cooling.

In this case, the last two integrals in Equation (26) vanish. Then the condition for axisymmetric *stability*, $\sigma^2 > 0$, is met if the integrand coefficients satisfy $A + D > 0$ and $AD - B^2 > 0$ (Ogilvie 2016, Section 11.6), which yields

$$\kappa^2 + \frac{1}{\rho_g}\nabla P\cdot\nabla f_d > 0, \qquad (28)$$

$$-\frac{1}{\rho_g}\frac{\partial P}{\partial z}\left(-\kappa^2\frac{\partial f_d}{\partial z} + r\frac{\partial\Omega^2}{\partial z}\frac{\partial f_d}{\partial r}\right) > 0, \qquad (29)$$

where $\kappa^2 \equiv r^{-3}\partial_r(r^4\Omega^2) > 0$ is the square of the epicyclic frequency. Note that $\nabla P/\rho_g = c_s^2\nabla\ln\rho_g$ for strictly isothermal gas considered here.

Equations (28)–(29) can in fact be obtained by inserting $C_P \ln(1 - f_d)$ for the entropy into the standard expression for the Solberg–Hoiland criteria (Tassoul 1978) for axisymmetric stability of adiabatic gas. This substitution is consistent with our definition of the effective entropy $S_{\rm eff}$ since we are considering constant c_s.

We expect Equation (28) to be satisfied in typical protoplanetary disks where the dust-to-gas ratio increases in the same direction as the local pressure gradient, which is equivalent to the gas density gradient for isothermal gas.

On the other hand, Equation (29) can be violated in disks if the dust is vertically well-mixed but radially stratified, such that $\partial_z f_d = 0$ but $\partial_r f_d \neq 0$. In this case the left of Equation (29) becomes

$$-\left(\frac{1}{\rho_g}\frac{\partial P}{\partial z}\right)^2 \left(\frac{\partial f_d}{\partial r}\right)^2 < 0. \tag{30}$$

Such an isothermal dusty disk is *unstable* because there is no effective vertical buoyancy to stabilize vertical motions ($N_z = 0$), which can tap into the free energy associated with vertical shear due to the radial gradient in the dust fraction. This situation is identical to the adiabatic simulations of Nelson et al. (2013) for pure gas, where the gas entropy is vertically uniform but has a radial gradient. The authors indeed find instability. We give a numerical example in the dusty context in Section 6.6.

4.4. Thermodynamics of Dust-drag Instabilities

The physical interpretation of Section 2 is here derived in detail. Consider constant c_s but $t_s \neq 0$ (so $\delta\mathcal{C} \neq 0$). Equation (26) indicates that σ^2 is generally complex, unless the second integral on the right is real. Thus we may have growing oscillations, or overstability, due to dust–gas friction. This is seen by taking the imaginary part of Equation (26):

$$s = \frac{\mathrm{Im} \int (\nabla \cdot \delta \boldsymbol{v}^*) \delta\mathcal{C} dV}{2\omega \mathcal{I}^2}, \tag{31}$$

assuming $\omega \neq 0$. Since drag ($\delta\mathcal{C}$) appears as a source term in our effective energy equation, the quantity $\mathrm{Im}[(\nabla \cdot \delta\boldsymbol{v}^*)\delta\mathcal{C}]$ represents correlations between compression/expansion and heating/cooling.

It is well known that such correlations may lead to pulsational instabilities in stars (Cox 1967). We thus interpret dust-drag overstabilities in a similar way, adapting from the treatment of stellar pulsations by Cox (1967) and lecture notes by Samadi et al. (2015) and J. Christensen-Dalsgaard.[4]

4.4.1. Work Done by Dusty Gas

The physical interpretation of Equation (31) is that work done by pressure forces in the dusty gas leads to growth ($s > 0$) or decay ($s < 0$) in oscillation amplitudes. To demonstrate this, we calculate the average work done assuming periodic oscillations, and show that if the average work done is positive, then the oscillation amplitude would actually grow.

---

[4] http://astro.phys.au.dk/~jcd/oscilnotes/print-chap-full.pdf

Consider oscillations in the dusty gas with period T_p. The average rate of work done is

$$\mathcal{W} = \frac{1}{T_p}\int_t^{t+T_p} dt' \int_M P\frac{D\upsilon}{Dt'}dm \tag{32}$$

(Cox 1967, see their Equation (4.10) and related discussions), where $\upsilon = 1/\rho$ is the specific volume of the mixture, D/Dt is the Lagrangian derivative, the spatial integral is taken over the total mass M of the mixture and dm is a mass element.

Here we consider Lagrangian perturbations such that

$$P \rightarrow P + \mathrm{Re}\left(\Delta P e^{-i\sigma t}\right) \tag{33}$$

is the pressure following a fluid element of the mixture (and similarly for ρ). The Lagrangian perturbation Δ of a variable X is $\Delta X = \delta X + \boldsymbol{\xi} \cdot \nabla X$ and $\boldsymbol{\xi}$ is the Lagrangian displacement, so $\xi_{x,z} = i\delta v_{x,z}/\sigma$. Inserting the above pressure and density fields into Equation (32), and noting that only products of perturbations contribute to $\mathcal{W}$ after time-averaging, we find for periodic oscillations (time dependence $e^{i\omega t}$ and real ω) that

$$\mathcal{W} = -\frac{\omega}{2}\int \mathrm{Im}\left(\Delta P\frac{\Delta\rho^*}{\rho}\right)dV, \tag{34}$$

Equation (34) shows that a phase difference between gas pressure and the total density leads to work done ($\mathcal{W} \neq 0$).

Now, Equations (67) and (68) imply that the integrand of the numerator in Equation (31) is

$$\mathrm{Im}(\delta\mathcal{C}\nabla \cdot \delta\boldsymbol{v}^*) = -|\sigma|^2\,\mathrm{Im}\left(\Delta P\frac{\Delta\rho^*}{\rho}\right), \tag{35}$$

for constant c_s. Then combining Equations (34), (35), and (31) gives

$$s = \frac{\mathcal{W}}{\mathcal{I}^2}, \tag{36}$$

where we have set $\sigma = -\omega$ in Equation (35). Equation (36) states that if the average work done is positive during an oscillation, $\mathcal{W} > 0$, then its amplitude will actually grow ($s > 0$).

Positive work is done by a fluid parcel if $-\omega\,\mathrm{Im}(\Delta P\Delta\rho^*) > 0$. Without loss of generality, take $\omega > 0$ and consider a mass element with $\Delta\rho = 1$. Then positive work requires $\mathrm{Im}(\Delta P) < 0$. This corresponds to Lagrangian pressure perturbations *lagging* behind those in density; see Figure 3 for the case of dusty gas.

4.4.2. Physical Properties of Overstabilities in Dust–Gas Drag

The above discussion applies to any single fluid with a pressure and density. In the case of interest—dusty gas—the work done is attributed to finite dust–gas drag. The relative drift between gas and dust, which only exists if $t_s\nabla P \neq 0$ (Equation (4)), causes a phase difference between the two components, and hence between pressure and total density.

A parcel of the strictly isothermal dusty gas mixture does positive work if

$$-\mathrm{sgn}(\omega)\,\mathrm{Im}(\Delta\rho_g\Delta\rho_d^*) > 0,$$

meaning that gas follows dust (Figure 3). Overstabilities are thus not possible if the gas does not respond to dust (i.e., no back-reaction). The pressure–density lag shown in Figure 3 is
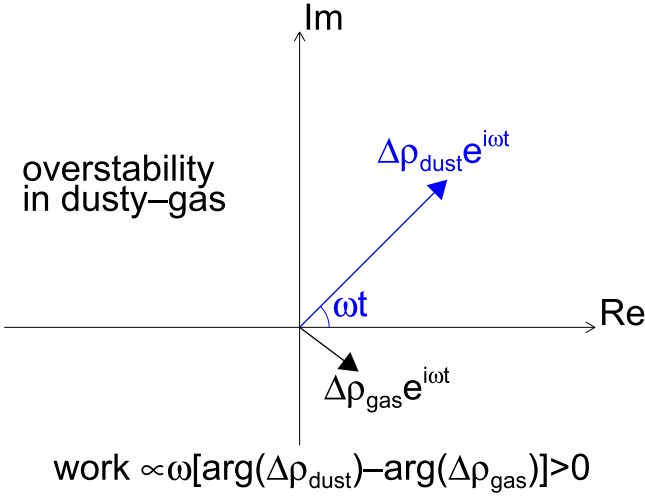
Figure 3. Phase relation for overstable modes in isothermal dusty gas. Such modes require (Lagrangian) oscillations in the gas pressure, which is directly proportional to the gas density, to lag behind those in dust density. The eigenvectors rotate anticlockwise for $\omega > 0$.

achieved if, just after the total density of a parcel maximizes, its gas content is increasing, which requires a sufficiently large particle flux *out* of the parcel. See A to B in Figure 2.

This thermodynamic interpretation does not explain why drag forces cause gas pressure to lag behind the dust density, but it shows that this *must* be the case for any growing oscillations associated with the dust–gas drag. To rigorously understand how dust drag causes this lag requires an explicit solution to the linearized equations with detailed treatment of the function $\mathcal{C}$. However, given the complexity of $\mathcal{C}$ (see Appendix C), we might generally expect dusty disks to support a range of stable and overstable modes, with the latter being associated with pressure–density lag. In Section 5.3.2 we check that the SI fits into this thermodynamic interpretation in the limit of strong drag.

4.5. Locally Isothermal Gas Perfectly Coupled to Dust

If $c_s(r, z)$ is nonuniform but $t_s = 0$, Equation (26) gives

$$s = \frac{\text{Im} \int P(\nabla \cdot \delta \mathbf{v}^*)(\delta \mathbf{v} \cdot \nabla \ln c_s^2) dV}{2\omega \mathcal{I}^2}, \qquad (37)$$

again assuming $\omega \neq 0$. This instability represents VSI caused by vertical shear arising from a radial temperature gradient (Nelson et al. 2013; Barker & Latter 2015; Lin & Youdin 2015). We present numerical solutions of the VSI with perfectly coupled dust in Section 6.

5. Application to Protoplanetary Disks

We now examine instabilities in dusty protoplanetary disks based on explicit descriptions of the equilibrium state. We first specify the disk structures to be analyzed. We show that sharp radial edges in the dust-to-gas ratio can render the disk unstable. We then revisit two well-known instabilities in dusty gas using the hydrodynamic framework developed thus far, namely SGI and the SI.

5.1. Disk Structure with a Prescribed Dust Distribution

We assume a Gaussian profile in the dust-to-gas ratio,

$$\epsilon(r, z) = \epsilon_0(r) \exp\left[-\frac{z^2}{2H_\epsilon^2(r)}\right]. \qquad (38)$$

Inserting Equation (38) into vertical hydrostatic equilibrium, Equation (22), and integrating with the approximate gravitational potential (Equation (10)), we obtain the gas density as

$$\rho_g(r, z)$$
$$= \rho_{g0}(r) \exp\left\{-\frac{z^2}{2H_g^2} - \epsilon_0 \frac{H_\epsilon^2}{H_g^2}\left[1 - \exp\left(-\frac{z^2}{2H_\epsilon^2}\right)\right]\right\}, \qquad (39)$$

where

$$H_g = \frac{c_s}{\Omega_K}, \qquad \Omega_K \equiv \sqrt{\frac{GM_*}{r^3}}. \qquad (40)$$

Here H_g is the gas scale-height in the dust-free limit and Ω_K is the Keplerian frequency.

In gas-dominated disks with $\epsilon_0 < 1$ the gas distribution $\rho_g(r, z)$ is close to Gaussian, as in the dust-free case, and the dust density is approximately

$$\rho_d \simeq \epsilon_0 \rho_{g0}(r) \exp\left(-\frac{z^2}{2H_d^2}\right), \qquad (41)$$

with

$$\frac{1}{H_d^2} = \frac{1}{H_\epsilon^2} + \frac{1}{H_g^2}, \qquad (42)$$

and H_d is the dust scale-height.

Finally, we define

$$Z \equiv \epsilon_0 \frac{H_d}{H_g} \simeq \frac{\Sigma_d}{\Sigma_g} \qquad (43)$$

as a measure of the local metallicity, where Σ_d and Σ_g are the dust and gas surface densities, respectively. The second equality holds for $\epsilon_0 \ll 1$.

5.1.1. Orbital Frequency

From Equation (21) the disk orbital frequency is

$$\Omega(r, z) = \Omega_K(r)\left[1 - \frac{3}{2}\frac{z^2}{r^2} + \frac{h_g^2}{(1 + \epsilon)}\frac{\partial}{\partial \ln r} \ln(c_s^2 \rho_g)\right]^{1/2}, \qquad (44)$$

where

$$h_g \equiv \frac{H_g}{r} \qquad (45)$$

is the characteristic disk aspect ratio, with $h_g \ll 1$ for protoplanetary disks (PPDs).

5.1.2. Vertical Shear

Writing Equation (23) in terms of the gas density and dust-to-gas ratio with a power-law temperature profile

(Equation (14)) gives the disk's explicit vertical shear profile:

$$
r\frac{\partial \Omega^2}{\partial z} = \frac{c_s^2(r)}{(1+\epsilon)^2}\left\{ \frac{\partial \epsilon}{\partial r}\frac{\partial \ln \rho_g}{\partial z} - \frac{\partial \epsilon}{\partial z}\frac{\partial \ln P}{\partial r} \right.
$$
$$
\left. - \frac{q}{r}(1+\epsilon)\frac{\partial \ln \rho_g}{\partial z} \right\}. \tag{46}
$$

The first two terms correspond to vertical shear caused by spatial variations in the dust-to-gas ratio. The third term proportional to q corresponds to vertical shear due to the radial temperature gradient, which survives in the dust-free limit.

We can compare these sources by evaluating them using the equilibrium solutions in Section 5.1. We assume the disk is radially smooth so that $\partial_r \sim 1/r$. This gives

$$
\frac{|r\partial_z\Omega|_{\text{dust/gas gradient}}}{|r\partial_z\Omega|_{\text{temp. gradient}}} \sim \epsilon \frac{\max(\delta^2, 1)}{|q|(1+\epsilon)\delta^2}, \tag{47}
$$

where $\delta \equiv H_\epsilon/H_g$. Since $|q| = O(1)$ in PPDs, Equation (47) indicates that vertical shear due to variations in the dust-to-gas ratio dominates over that due to the radial temperature gradient for thin dust layers such that $\delta^2 \ll \epsilon$.

5.1.3. Dusty Vertical Buoyancy

For the above equilibrium the vertical buoyancy frequency is given explicitly as

$$
N_z^2 = \frac{\epsilon}{(1+\epsilon)^2}\left(\frac{z}{H_\epsilon}\right)^2 \Omega_K^2,
$$

where we have used $c_s = c_s(r)$. Then

$$
N_z \lesssim O(\sqrt{\epsilon_0}\,\Omega_K).
$$

However, for well-mixed dust layers such that $H_\epsilon \gg H_g$, $\max(N_z)$ may occur outside a finite vertical domain.

5.2. Instability of Dusty Edges

Here we apply the dusty analog of the Solberg–Hoiland criteria derived in Section 4.3 assuming strictly isothermal gas. As discussed there, the first criterion is generally satisfied. Thus we only consider the second condition, Equation (29).

We assume that the disk is approximately Keplerian so that $\kappa \simeq \Omega_K$, and that the vertical gas distribution is Gaussian. In terms of the dust-to-gas ratio ϵ, Equation (29) becomes

$$
1 - \frac{\epsilon h_g^2}{(1+\epsilon)^2}\frac{\partial \ln \epsilon}{\partial \ln r}\left(-\frac{\partial \ln P}{\partial \ln r} + \frac{H_\epsilon^2}{H_g^2}\frac{\partial \ln \epsilon}{\partial \ln r} \right) > 0, \tag{48}
$$

for *stability*. The first term in brackets is usually stabilizing in PPDs for reasons given in Section 4.3. The second term in brackets is always destabilizing, but is small in smooth, thin disks with radial gradients $O(1/r)$, $h_g \ll 1$, provided that H_ϵ/H_g is not large (e.g., some dust settling has occurred). This means that typical dusty PPDs are stable to axisymmetric perturbations, even for arbitrarily thin dust layers.

To violate Equation (48) and obtain instability, notice that the left side is a quadratic in $\partial_r\epsilon$. Thus instability is possible for sufficiently large (in magnitude) radial gradients in the

dust-to-gas ratio,

$$
\frac{\partial \ln \epsilon}{\partial \ln r} > \chi_+ \quad \text{or} \quad \frac{\partial \ln \epsilon}{\partial \ln r} < \chi_-, \tag{49}
$$

for *instability*, where

$$
\chi_\pm = \frac{1}{2}\frac{H_g^2}{H_\epsilon^2}\left[\frac{\partial \ln P}{\partial \ln r} \pm \sqrt{\left(\frac{\partial \ln P}{\partial \ln r}\right)^2 + 4\frac{H_\epsilon^2}{H_g^2}\frac{(1+\epsilon)^2}{\epsilon h_g^2}} \right]. \tag{50}
$$

In typical accretion disks where $\partial_r P < 0$, instability is easier for increasing dust-to-gas ratios ($\partial_r \epsilon > 0$).

We can neglect pressure gradients in Equation (50) if $r\partial_r \ln P \sim O(1)$ and $H_\epsilon/H_g \gg \sqrt{\epsilon}h_g/2(1+\epsilon)$. For example, if $\epsilon \simeq 0.01$ and $h_g \simeq 0.05$, then we require $H_\epsilon/H_g \gg 2 \times 10^{-3}$. This can be met if the dust is not well settled (e.g., due to a small amount of turbulence). Then instability requires

$$
\left| \frac{\partial \ln \epsilon}{\partial r} \right| \gtrsim \frac{1}{H_\epsilon}\frac{(1+\epsilon)}{\sqrt{\epsilon}}. \tag{51}
$$

That is, if the radial lengthscale of the dust-to-gas ratio is much less its vertical lengthscale, $L_\epsilon \ll O(H_\epsilon)$, then the system is unstable. Taking $\epsilon \sim 0.01$, we find that for thin dust layers with $H_\epsilon \simeq H_d \ll H_g$, instability requires $L_\epsilon \ll O(0.1H_g)$, i.e., the dust-to-gas ratio must vary on an extremely short radial lengthscale. This might be achieved, for example, at sharp edges associated with gaps opened by giant planets.

Technically, the above discussion is applicable only when c_s is constant and $t_s = 0$ (see Section 4.3). However, since dusty edges translate to sharp entropy gradients (Section 3.3), we may generally expect sharp features in the dust distribution of protoplanetary disks to be unstable.

5.3. Radially Local Problem

We now specialize further and compute explicit solutions to the linear problem. We consider radially localized axisymmetric disturbances of the form

$$
\delta X(r, z) = \delta X_1(r, z)\exp(ik_x r), \tag{52}
$$

where k_x is a real wavenumber such that $|k_x r| \gg 1$, and the amplitude $\delta X_1(r, z)$ is a slowly varying function of r. Then $\partial_r \to ik_x$ when acting on the above primitive perturbations, and we may neglect curvature terms. We take $k_x > 0$ without loss of generality. Hereafter, we drop the subscript 1 on the amplitudes.

Introducing

$$
W \equiv \frac{\delta\rho}{\rho}, \quad Q \equiv \frac{\delta P}{\rho}, \tag{53}
$$

the linearized equations for vertically isothermal dusty gas with the pressure equation in place of the dust fraction (Equations (5), (7), (11), (15)) are then

$$
i\sigma W = ik_x \delta v_r + \delta v_z' + \delta v_r \partial_r \ln \rho + \delta v_z \partial_z \ln \rho, \tag{54}
$$

$$
-i\sigma \delta v_r = 2\Omega \delta v_\phi - WF_r - ik_x Q - ik_x \delta\psi, \tag{55}
$$

$$
i\sigma \delta v_\phi = \frac{\kappa^2}{2\Omega}\delta v_r + \frac{\partial v_\phi}{\partial z}\delta v_z, \tag{56}
$$

$$
-i\sigma \delta v_z = -WF_z - [Q' + Q(\ln \rho)'] - \delta\psi', \tag{57}
$$

$$i\sigma Q = \frac{P}{\rho}(ik_x\delta v_r + \delta v_z') + \frac{1}{\rho}(\delta v_r \partial_r P + \delta v_z \partial_z P)$$
$$- \frac{P}{\rho}\delta v_r \partial_r \ln c_s^2 - \frac{\delta\mathcal{C}}{\rho}, \tag{58}$$

$$\delta\psi'' = 4\pi G\rho W + k_x^2 \delta\psi, \tag{59}$$

where $' \equiv \partial_z$ and recall $\boldsymbol{F} \equiv -\nabla P/\rho$. We have temporarily restored self-gravity to discuss SGI in the next section. The linearized dust diffusion function $\delta\mathcal{C}$ is given in Appendix C.

Equations (54)–(59) are a set of ordinary differential equations in z. All coefficients and amplitudes are evaluated at a fiducial radius $r = r_0$, but their full z-dependence is retained. We next discuss solutions to these equations. We first show that the above equations yield the SGI and SI in the strong drag regime in Sections 5.3.1 and 5.3.2, respectively. We then consider 3D, stratified disks in Section 6 to study how the addition of dust affects the VSI.

5.3.1. Secular Gravitational Instability

Consider a razor-thin, self-gravitating disk so that $\rho = \Sigma\delta(z)$, where δ is the Dirac delta function and Σ is the total surface density. Here $\epsilon = \Sigma_d/\Sigma_g$ and $f_d = \Sigma_d/\Sigma$, where $\Sigma_{d,g}$ are the dust and gas surface densities. The background disk is uniform and we neglect the vertical dimension in Equations (54)–(58). The linearized dust–gas drag term is then $-\delta\mathcal{C}/\rho = t_s f_d c_s^2 k_x^2 Q$. The thin-disk solution to Equation (59) is $\delta\psi(z = 0) = -2\pi G\Sigma W/|k_x|$.

These simplifications yield the dispersion relation

$$(i\sigma - t_s f_d c_s^2 k_x^2)(2\pi G\Sigma|k_x| - \kappa^2 + \sigma^2) = i\sigma c_s^2 k_x^2(1 - f_d).$$

Searching for slowly and purely growing modes, $\sigma = is$ with $|s| \ll \kappa$, we find

$$s = \frac{t_s f_d c_s^2 k_x^2 (2\pi\Sigma G|k_x| - \kappa^2)}{\kappa^2 - 2\pi\Sigma G|k_x| + c_s^2 k_x^2(1 - f_d)}. \tag{60}$$

This is SGI mediated by strong dust–gas drag with negligible turbulent dust diffusion (Takahashi & Inutsuka 2014, their Equation (13) becomes our Equation (60) in this limit after a change of variables). A similar effect occurs in viscous self-gravitating gas disks (Gammie 1996; Lin & Kratter 2016). In fact, if we identify $\nu \equiv t_s f_d c_s^2$ as a kinematic viscosity, then Equation (60) is identical to Gammie's Equation (18).

This exercise shows that the one-fluid framework, further simplified by the terminal velocity approximation, is sufficient to capture SGI in the limit of strong drag.

5.3.2. Streaming Instability

We now consider 3D disks without self-gravity. We neglect the vertical component of the stellar gravity, appropriate for studying regions near the disk midplane. This allows us to Fourier analyze in z to obtain an algebraic dispersion relation of the form $\sum_{j=0}^{5} c_j(k_x, k_z)\sigma^j = 0$, where k_z is a real vertical wavenumber. The coefficients c_j can be read off Equation (96) in Appendix D. There we also show that this dispersion relation reduces to that for the SI in the limit of incompressible gas and small t_s (Youdin & Goodman 2005; Jacquet et al. 2011).

In Table 1 we solve the full dispersion relation (Equation (96)) numerically for selected cases where analytic SI growth rates have been verified with particle–gas numerical

simulations (from Youdin & Johansen 2007; Bai & Stone 2010b). Following previous works on SI, we use normalized wavenumbers $K_{x,z} = \eta r k_{x,z}$ where

$$\eta \equiv -\frac{1}{2\rho_g r\Omega_K^2}\frac{\partial P}{\partial r} = \frac{1}{2(1-f_d)}\frac{F_r}{r\Omega_K^2} \tag{61}$$

measures the pressure offset of Keplerian rotation. We fix $\eta = 0.05 c_s/r\Omega_K$. In this section we also quote the particle stopping time $\tau_s = t_s/(1 - f_d)$.

The eigenfrequencies obtained from the one-fluid dispersion relation are compared with those from a full, two-fluid analysis (similar to Youdin & Goodman 2005; Kowalik et al. 2013). As expected, eigenfrequencies agree better with decreasing τ_s since in that limit the mixture behaves more like a single fluid. Most importantly, we find the work done $\mathcal{W} > 0$ in all cases, and hence find growing oscillations.

In Table 1 we also calculate the phase difference between the Lagrangian pressure perturbation and density perturbations as

$$\varphi \equiv \mathrm{sgn}\,[\mathrm{Re}(\sigma)]\arg(\Delta P\Delta\rho^*).$$

(Note that it is important to include the global radial pressure gradient in $\Delta P = \delta P + i\delta v_x \partial_r P/\sigma$.) Then $\varphi > 0$ indicates gas pressure lagging behind total density, which is true for all the cases. Thus SI is indeed associated with such a phase lag.

In Figure 4 we calculate the most unstable SI mode as a function of τ_s at fixed $K_z = 30$ and $\epsilon = 3$. Growth rates are maximized over K_x. We compare results between the full, two-fluid linear analysis and the one-fluid framework. We also include an analytic model, developed in Appendix D.2, based on the one-fluid dispersion relation with additional approximations (orange diamonds).

Both results based on the one-fluid framework compare well with the full, two-fluid analysis, only breaking down at a relatively large $\tau_s\Omega_K \gtrsim 0.1$. For larger τ_s the two-fluid phase lag drops, along with the growth rate. This suggest that a non-vanishing phase lag is indeed necessary for instability. However, the magnitude of the phase lag does not correlate with growth rates. In fact, φ remains finite as $|\sigma|$, $\tau_s \rightarrow 0$ (but non-zero). This arises because the optimum $K_x \propto \tau_s^{-1/2}$ diverges (see Appendix D.2).

In a future work we will perform a more detailed parameter survey to compare the simplified one-fluid and full two-fluid frameworks in calculating SI (see comparisons using other problems, Laibe & Price 2014; Price & Laibe 2015).

6. VSI with Dust

We now present numerical solutions for vertically stratified, non-self-gravitating disks, assuming perfectly coupled dust. We formally take $t_s = 0$ so the equilibrium solutions defined in Section 4.1 are exact steady states. In reality, dust settles to the midplane on a timescale $t_{settle} \sim 1/t_s\Omega_K^2$ (Takeuchi & Lin 2002). However, we expect the perfectly coupled limit to be valid provided timescales of interest $t_{grow} \ll t_{settle}$. For the VSI this translates to $t_s\Omega_K \ll h_g$. For thin PPDs, this is satisfied for $t_s\Omega_K \ll O(10^{-2})$.

We first consider constant midplane dust-to-gas ratios ϵ_0 and characteristic thickness H_ϵ. Then the dust-to-gas ratio $\epsilon = \epsilon(z)$. In this limit any growing modes must be associated with the imposed temperature gradient (see Section 4). We then study the effect of dust-loading on the VSI previously studied in pure gas disks (Lin & Youdin 2015, LY15 in this section). In

Table 1
Selected Modes of the Streaming Instability

Mode ($\tau_s\Omega_K$, $K_{x,z}$, ρ_g/ρ_d)	Complex Frequency, σ/Ω_K		Work Done, $\mathcal{W}/|\Delta P \Delta \rho^*/\rho|$		Pressure–density lag, φ	
	Two-fluid	One-fluid	Two-fluid	One-fluid	Two-fluid	One-fluid
linA (1) (0.1, 30, 3)	$0.3480 + 0.4190i$	$0.3640 + 0.4249i$	0.078	0.090	27°	30°
linB (1) (0.1, 6, 0.2)	$-0.4999 + 0.0155i$	$-0.4981 + 0.0054i$	0.025	0.0054	5°.8	1°.2
linC (2) (10^{-2}, 1500, 2)	$0.1049 + 0.5981i$	$0.1338 + 0.6650i$	0.0076	0.013	8°.3	11°
linD (2) (10^{-3}, 2000, 2)	$0.3225 + 0.3154i$	$0.3219 + 0.3154i$	0.061	0.061	22°	22°

References. (1) Youdin & Johansen (2007); (2) Bai & Stone (2010b).
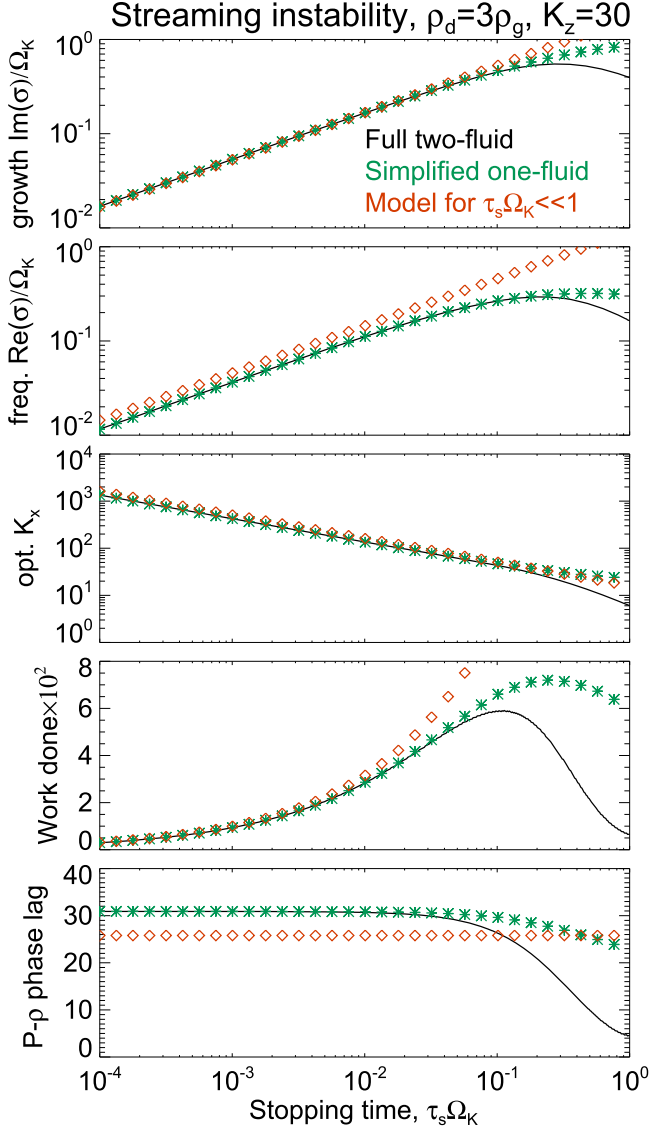
Figure 4. Comparison of the linear streaming instability between a full two-fluid analysis (solid line), the one-fluid framework simplified by the terminal velocity approximation (green asterisks), and an analytic solution to the one-fluid dispersion relation in the dust-rich limit (orange diamonds, see also Appendix D.2). The vertical wavenumber is fixed and growth rates are maximized over K_x.
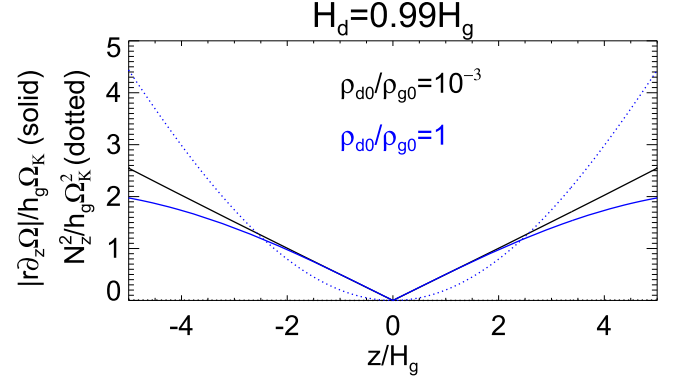

Figure 5. Vertical shear rate (solid) compared to vertical buoyancy (dotted) in a locally isothermal, dusty disk with midplane dust-to-gas ratio of $\epsilon_0 = 10^{-3}$ (black) and $\epsilon_0 = 1$ (blue). The dust layer thickness is fixed at $H_d = 0.99 H_g$ so the dust-to-gas ratio ϵ is approximately constant with height. Vertical buoyancy here is due to dust-loading.

We choose a midplane gas density profile $\rho_{g0} \propto r^{-3/2}$. The fiducial power-law index for the temperature profile is $q = -1$; and we set the aspect ratio of the gas disk to be $h_g = 0.05$. These values were also used by LY15.

We impose solid vertical boundaries so that $\delta v_z(\pm z_{max}) = 0$. We solve the linearized equations as a generalized eigenvalue problem using a pseudo-spectral code adapted from LY15. Amplitudes are expanded in Chebyshev polynomials up to order 512.

6.1. Qualitative Expectations

LY15 found that the appropriate way to compare vertical shear (destabilizing) and vertical buoyancy (stabilizing) is $r\partial_z\Omega/\Omega_K$ against N_z^2/Ω_K^2. From Sections 5.1.2 and 5.1.3 we find $|r\partial_z\Omega| \sim qh_g\Omega_K$ for a thin, gas-dominated disk, while $N_z^2 \sim \epsilon\Omega_K^2$. Thus we expect dust-induced buoyancy forces to stabilize the disk against the VSI where $\epsilon \gtrsim h_g$.

6.2. Effect of Dust-loading

We first vary the midplane dust-to-gas ratio $\epsilon_0 \in [10^{-3}, 1]$, fixing the dust thickness to $H_d = 0.99 H_g$. Then ϵ is roughly constant with height. We set the vertical domain to $z_{max} = 5H_g$.

Figure 5 compares the vertical shear rate in the basic state, which is destabilizing, and the vertical buoyancy frequency, which is stabilizing. For the nearly dust-free disk with $\epsilon_0 = 10^{-3}$ the vertical shear dominates buoyancy for all $|z| > 0$. However, a heavy dust-load with $\epsilon_0 = 1$ causes the buoyancy to dominate over vertical shear in the disk atmosphere $|z| \gtrsim 2.5 H_g$. We thus expect instability to occur
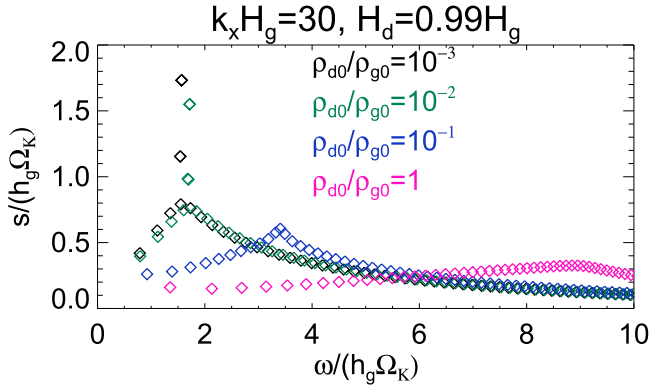
Section 6.5 we allow $\partial_r\epsilon \neq 0$, and in Section 6.6 we consider VSI driven entirely by radial gradients in the dust-to-gas ratio (as discussed in Section 4.3).

The parameters for the linear problem includes ϵ_0, the dust layer thickness H_d, and the perturbation radial wavenumber k_x.

Figure 6. Unstable modes in a locally isothermal, perfectly coupled dusty disk with fiducial parameters $(p, q, h_g, H_d/H_g) = (-1.5, -1, 0.05, 0.99)$. The real frequency ω and growth rates s are shown for a range of midplane dust-to-gas ratios $\epsilon_0 = \rho_{g0}/\rho_{d0}$.
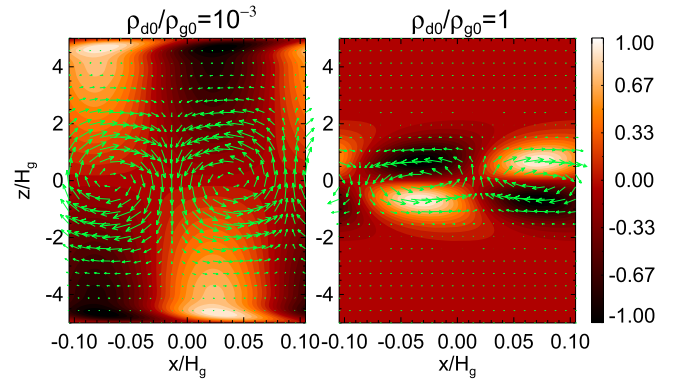

Figure 7. Fundamental dusty VSI mode in real space for midplane dust-to-gas ratio $\epsilon_0 = 10^{-3}$ (left) and $\epsilon_0 = 1$ (right). The color scale shows the perturbation to the dust-to-gas ratio, $\delta\epsilon$; and the arrows show $\sqrt{\rho}(\delta v_x, \delta v_z)$.

at all heights for $\epsilon_0 = 10^{-3}$, but to be restricted to the midplane for $\epsilon_0 = 1$.

Figure 6 shows unstable modes for different values of ϵ_0 with fixed perturbation wavenumber $k_x H_g = 30$. The eigenvalue distributions for $\epsilon_0 \leqslant 10^{-2}$ are similar to the dust-free fiducial case considered by LY15. This is expected since $\epsilon_0 < h_g$ (Section 6.1). Eigenvalues consists of the roughly horizontal "body modes," and the nearly vertical "surface modes" (which are associated with the imposed vertical boundaries, Barker & Latter 2015).

We find that increasing the dust-to-gas ratio reduces VSI growth rates. Notably, surface modes, which are typically fastest growing in the dust-free case, are suppressed in dusty disks for $\epsilon_0 \geqslant 0.1$ (i.e., $\epsilon_0 > h_g$). The body modes' growth rates remain $O(h_g\Omega_K)$ but their oscillation frequency increases with dust-loading, i.e., it increases with the vertical buoyancy. The total number of modes does not change significantly. This is in contrast with the effect of increasing cooling times in an adiabatic gas disk, for which LY15 find fewer unstable modes.

The lowest frequency "fundamental" body mode is energetically dominant because the entire disk column is perturbed (unlike surface modes, which only disturb the disk boundaries, Umurhan et al. 2016a). In Figure 7 we compare the fundamental mode between the nearly dust-free case $\epsilon_0 = 10^{-3}$ and a dusty disk with $\epsilon_0 = 1$. Dust-loading preferentially stabilizes the disk atmosphere against the VSI, restricting meridional motions to $|z| \lesssim 2H_g$. This is consistent with Figure 5 comparing the vertical shear in the basic state and the buoyancy.

In Figure 8 we plot the growth rates as a function of ϵ_0 for different perturbation wavenumbers k_x. Dust-loading stabilizes the VSI more effectively for shorter wavelength perturbations. This is because for high wavenumbers the dominant modes are surface modes, which are effectively stabilized by dust-loading because buoyancy forces are largest near the vertical boundaries. The figure suggest that VSI becomes much less efficient for $\epsilon_0 \gtrsim 0.1$ and $k_x H_g \gtrsim 50$.

6.3. Effect of Dust Layer Thickness

We now vary H_d but fix the metallicity $Z \equiv \epsilon_0 H_d/H_g = 0.03$ to obtain ϵ_0. Since we will consider thin dust layers, here we use a smaller domain with $z_{max} = 2H_g$ so that ϵ does not become too small.
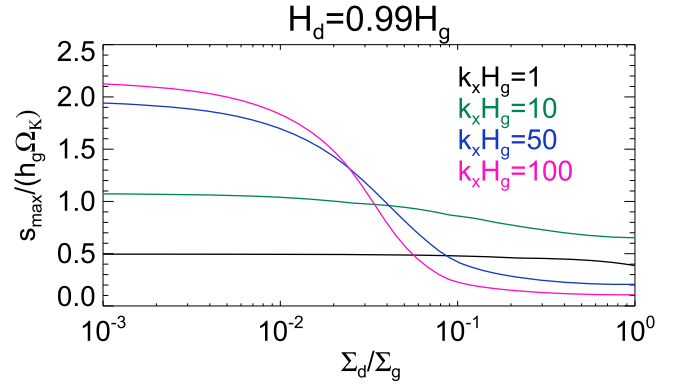
Figure 8. Maximum growth rate of the dusty VSI as a function of the midplane dust-to-gas ratio ϵ_0 for perturbations with different radial wavenumbers k. The dust layer thickness is fixed at $H_d \simeq H_g$.
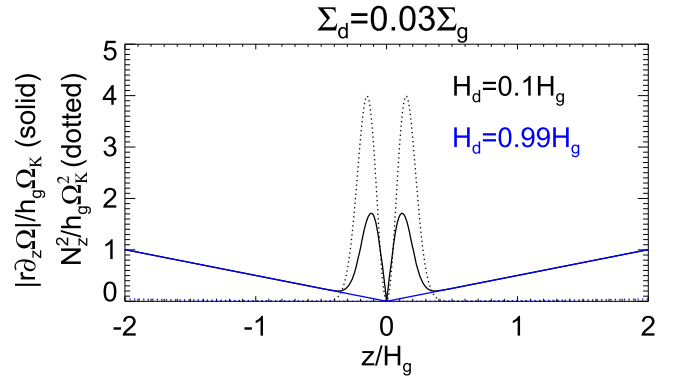

Figure 9. Vertical shear rate (solid) compared to vertical buoyancy (dotted) in a locally isothermal, dusty disk with metallicity $Z = 0.03$ and dust thickness $H_d = 0.1H_g$ (black) and $H_d = 0.99H_g$ (blue).

We analyze two disks with $H_d = 0.1H_g$ and $H_d = 0.99H_g$. Figure 9 compares the vertical shear rate and buoyancy frequency. For $|z| \gtrsim 0.4H_g$ the two disks have the same profile, with vertical shear dominating over buoyancy. We thus expect perturbations away from the disk midplane in both cases. For $|z| \lesssim 0.4H_g$, a thin dust layer with $H_d = 0.1H_g$ boosts the vertical shear rate, but the associated buoyancy is larger still, implying that the midplane should be stable.

Figure 10 compares the fastest growing VSI body modes with $k_x H_g = 30$ for the two cases above. (The thinner domain adopted here eliminates surface modes, LY15.) We find very
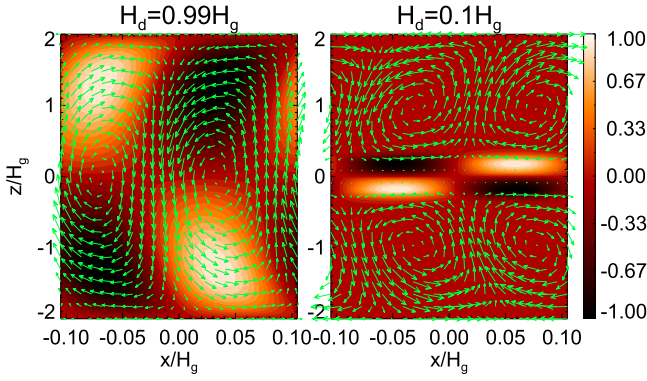
Figure 10. Fastest growing dusty VSI mode in real space for midplane dust layer thickness $H_d = 0.99H_g$ (left) and $H_d = 0.1H_g$ (right). The dust content is fixed at $\Sigma_d = 0.03\Sigma_g$. The color scale shows the perturbation to the dust-to-gas ratio, $\delta\epsilon$; and the arrows show $\sqrt{\rho}\,(\delta v_x, \delta v_z)$.

similar mode frequencies

$$\sigma = \begin{cases} (0.3053i - 0.8142)h_g\Omega_K & H_d = 0.99H_g, \\ (0.3178i - 1.2237)h_g\Omega_K & H_d = 0.1H_g, \end{cases}$$

since the vertical shear profile is similar throughout most of the disk. However, meridional motions are suppressed near the midplane of the $H_d = 0.1H_g$ disk, as expected from the larger buoyancy frequency relative to vertical shear there. This leads to a structure analogous to PPD dead zones: a quiescent midplane between active surface layers (Gammie 1996).

Figure 11 shows the maximum VSI growth rates as a function of H_d. As before, we find that growth rates are most affected by the vertical structure of the dust layer when the perturbation wavenumber is large. Notice that VSI growth rates converge as $H_d \to 0$. Thus a thin dust layer, however large its associated vertical shear, does not affect VSI growth rates. The non-monotonic behavior for $H_d \gtrsim 0.5H_g$ arises because the vertical buoyancy frequency

$$N_z^2(H_d; z, Z) \simeq ZH_g z^2 \exp\left(-\frac{z^2}{2H_g^2}\right)\Omega_K^2$$

$$\times \frac{1}{H_d}\left(\frac{1}{H_d^2} - \frac{1}{H_g^2}\right)\exp\left(-\frac{z^2}{2H_d^2}\right)$$

is a non-monotonic function of H_d at fixed z. At $z = H_g$ and $z = 2H_g$ the buoyancy frequency is maximized for $H_d \simeq 0.5H_g$ and $H_d \simeq 0.8H_g$, respectively. This is consistent with the minima in growth rates in Figure 11.

6.4. Axisymmetric Stability of Ultrathin Dust Layers

The discussion in Section 4.3 implies that strictly isothermal disks with a radially uniform dust-to-gas ratio are stable against axisymmetric perturbations, no matter how thin the dust layer is. We now demonstrate this numerically.

To connect with similar studies, here we also use the Richardson number $\text{Ri} \equiv N_z^2/(r\partial_z\Omega)^2$ to label calculations (Youdin & Shu 2002). Numerical simulations show that non-axisymmetric instabilities develop when $\text{Ri} \lesssim 0.1$, brought about by very thin dust layers (Chiang 2008; Lee et al. 2010). We show that *axisymmetric* instabilities never develop in radially uniform disks, however small Ri.
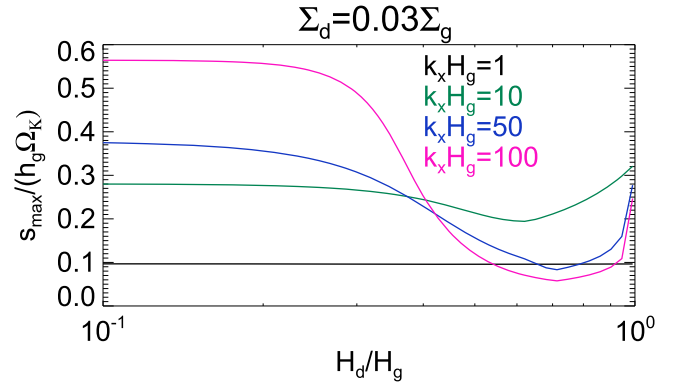

Figure 11. Maximum VSI growth rate for different perturbation wavenumbers k as a function of the dust layer thickness H_d at fixed metallicity $Z = 0.03$.
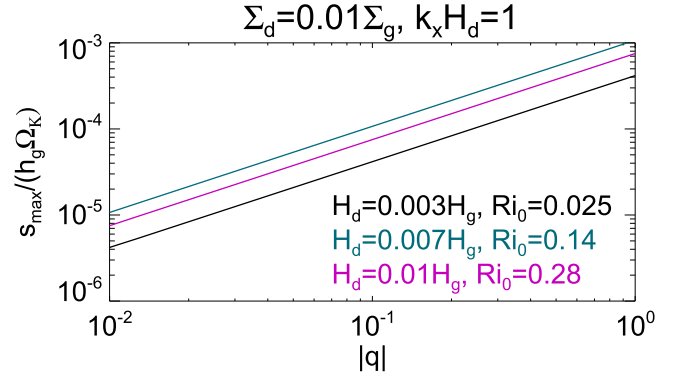

Figure 12. Maximum VSI growth rate for ultrathin dust layers $H_d \leqslant 0.01H_g$ (with radially uniform dust-to-gas ratio). Vertical shear is dominated by that due to vertical dust stratification, but axisymmetric instability is still associated with the radial temperature gradient q. Here, Ri_0 is the minimum Richardson number in the domain in the limit $q \to 0$. The disk is stable to axisymmetric perturbations in the strictly isothermal limit, regardless of the dust layer thickness.

We shall consider ultrathin dust layers with $H_d \leqslant 0.01H_g$ and thus restrict the vertical domain to $z_{\max} = 0.02H_g$. We fix the metallicity at $Z = 0.01$ so the midplane dust-to-gas ratio ϵ_0 is $O(1)$. We consider radial wavenumbers with $k_x H_d = 1$.

Figure 12 shows the maximum growth rate as a function of the radial temperature gradient, q. For all cases the vertical shear is dominated by that due to the dust layer (see Section 5.1.2). However, we see that $s \propto |q|$, i.e., growth rates vanish in the strictly isothermal limit. In particular, this holds for $\text{Ri} < 0.1$, the critical value for non-axisymmetric instabilities.

Axisymmetric instability here is associated with the thermal contribution to vertical shear: as $q \to 0$, $\partial_z\Omega$ becomes entirely due to $\partial_z\epsilon$ and there is no instability ($s \to 0$). This result is independent of Ri, so the Richardson number does not characterize the axisymmetric stability of dust layers.

6.5. Effect of a Radially Varying Dust-to-gas Ratio

We now consider a radially varying dust-to-gas ratio. Specifically we let $\epsilon_0 \propto r^{-1}$ and $H_\epsilon \propto H_g$ (compare with constant values in the previous calculations). Then

$$\frac{\partial\epsilon}{\partial r} = \left(\frac{z^2}{H_\epsilon^2}\frac{d\ln H_g}{dr} - \frac{1}{r}\right)\epsilon.$$

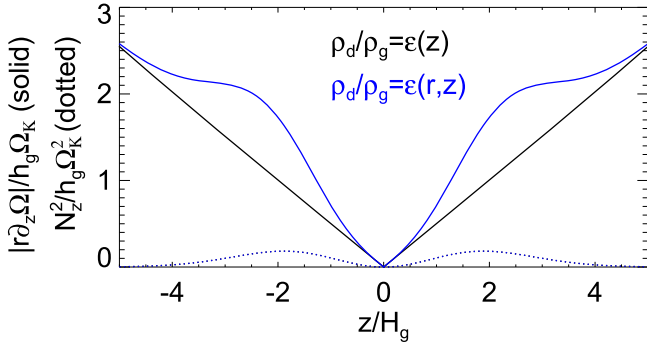Here we fix $Z = 0.01$ and $H_d = 0.8H_g$.

Figure 13. Vertical shear rate (solid) compared to vertical buoyancy (dotted) in a locally isothermal, dusty disk with metallicity $Z = 0.01$ and dust thickness $H_d = 0.8H_g$. Black curves assume a dust-to-gas ratio that depends only on height, whereas the blue curve also allows a radial dependence in ϵ. See text for details.

Figure 13 shows that a radially varying dust-to-gas ratio increases the magnitude of the vertical shear rate away from the midplane (see also Equation (46)). Thus we typically find higher VSI growth rates, as shown in Figure 14. Surfaces modes, appearing at high k_x, are more effectively enhanced by the additional vertical shear induced by $\partial_r \epsilon$. Low-frequency body modes with small k_x are more affected by radial variations in the dust-to-gas ratio than high-frequency body modes with high k_x.

However, all growth rates remain $O(h_g \Omega_K)$. Importantly, the increase in the growth rate of the fundamental mode is small. We do not expect the radial dependence in ϵ to significantly affect the VSI in a dusty disk.

6.6. Pure Instability with Vertically Well-mixed Dust

In Section 4.3 we found that for strictly isothermal disks, a vertically uniform dust-to-gas ratio can be unstable if $d\epsilon/dr \neq 0$. To demonstrate this numerically we set $q = 0$ and H_d such that $H_\epsilon = 10^3 H_g$. We let $\rho_d/\rho_g \propto r^{-d}$ with different power indices d. The metallicity is fixed at $Z = 0.03$. In these cases vertical shear $\partial_z \Omega$ is attributed to the radially varying dust-to-gas ratio (see Equation (46)).

We show unstable modes in Figure 15. As expected from the discussion in Section 4.3, the disk admits purely growing modes with $\omega = 0$. This is distinct from the growing oscillations associated with classic VSI discussed above.

We find that in smooth disks large k_x is needed for appreciable growth rates, e.g., $k_x H_g = 1800$ with $\rho_d/\rho_g \propto r^{-1}$. Local shearing-box simulations may be required to study the nonlinear evolution of such short wavelengths (e.g., Bai & Stone 2010b; Yang & Johansen 2016). Alternatively, as shown in Figure 15, a rapidly varying dust-to-gas ratio permits dynamical instability at longer radial wavelengths, which might be resolvable in global disk simulations.

7. Discussion

7.1. Applications and Limitations

The main application we envision for the dusty/adiabatic gas analogy is to develop physical interpretations of dust–gas drag instabilities, and to find dusty analogs of pure gas instabilities in protoplanetary disks, which is discussed in Section 7.3. One can also exploit the similarity to adapt existing hydrodynamic codes to simulate dusty protoplanetary disks (see Section 7.4).
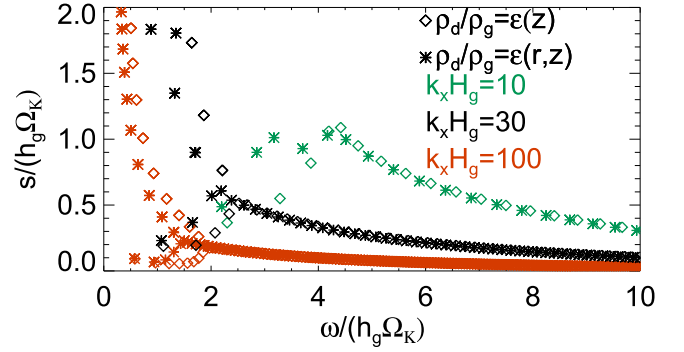

Figure 14. Unstable VSI modes in the disk models of Figure 13. Diamonds (asterisks) are mode frequencies for a disk with radially uniform (varying) dust-to-gas ratio. The radial wavenumbers are $k_x H_g = 10$ (green), $k_x H_g = 30$ (black), and $k_x H_g = 100$ (orange).
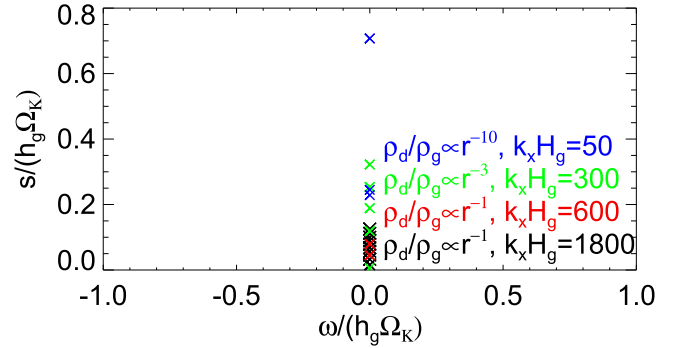

Figure 15. Purely growing modes in a strictly isothermal disk ($q = 0$) with vertically uniform dust-to-gas ratio. The instability is due to vertical shear $\partial_z \Omega \neq 0$ arising from radial variations in the dust-to-gas ratio, $d\epsilon/dr \neq 0$.

It is important to keep in mind the assumptions used to develop our thermodynamic model of dusty gas. The terminal velocity approximation, $v_d - v_g = t_s \nabla P/\rho_g$, was employed from the outset. This is applicable to small particles with short stopping times that are strongly coupled to the gas. Generally we require t_s to be the shortest timescale in the physical problem. For example, to study dust settling, we require $t_s \ll t_{settle} \sim 1/t_s \Omega_K^2$, or $t_s \Omega_K \ll 1$.

However, the validity of the terminal velocity approximation may depend not only on t_s. The value of the dust–gas ratio and the problem itself may also be important. For example, Table 1 shows that the dust-rich "linA" mode and dust-poor "linB" mode of the SI have the same t_s, but the former is accurately captured by the simplified equations, while the latter is not. This suggests that for the SI the simplified equations are better suited for $\rho_d/\rho_g > 1$. The simplified equations also contain spurious modes in certain limits (see Appendix D.3).

Note that our thermodynamic interpretation of dust–gas drift does *not* actually depend on the terminal velocity approximation. Once the equation of state for the gas is fixed and the true energy equation deleted, the dust continuity equation can be converted to a new effective energy equation. As an example, for strictly isothermal dusty gas we obtain

$$\frac{DP}{Dt} = -P\nabla \cdot \boldsymbol{v} + c_s^2 \nabla \cdot [f_d(1-f_d)\rho(\boldsymbol{v}_d - \boldsymbol{v}_g)]. \quad (62)$$

This equation does not use the terminal velocity approximation (which gives Equation (15)). Evaluating the right side generally requires solving an evolutionary equation for $\boldsymbol{v}_d - \boldsymbol{v}_g$ (Laibe &

Price 2014). Nevertheless, Equation (62) shows that dust–gas relative drift can be interpreted as a heat flux within the dust–gas mixture. Thus, even without the terminal velocity approximation we can regard the dusty gas as a single ideal fluid subject to cooling.

7.2. Generalization to Locally Polytropic Disks

We can extend the correspondence between dusty and adiabatic gas to other fixed equations of state. As an example, consider the locally polytropic disk

$$P = K(r, z)\rho_g^\Gamma, \tag{63}$$

where K is a prescribed function and Γ is the constant polytropic index. Then eliminating f_d from the dust Equation (6) gives

$$\frac{DP}{Dt} = -\Gamma P \nabla \cdot \boldsymbol{v} + P\boldsymbol{v} \cdot \nabla \ln K + \frac{\Gamma P}{\rho_g} \nabla \cdot (f_d t_s \nabla P). \tag{64}$$

Thus the dusty gas behaves like a pure gas with adiabatic index Γ. The entropy is given by

$$S_{eff} = \ln[K^{1/\Gamma}(r, z)(1 - f_d)]. \tag{65}$$

The results of Sections 4.3 and 4.4 remain valid for the strictly polytropic disk with K = constant, while one sets $c_s^2 \to K$ in Section 4.5.

7.3. Dusty Analogs of Other Gaseous Instabilities

7.3.1. Classic GIs

The addition of dust enhances GI because dust particles contribute to the total disk mass but not thermal pressure, which effectively lowers the disk temperature (Thompson & Stevenson 1988; Shi & Chiang 2013). For typical dust-loading f_d with $Z \ll 1$, this effect is unimportant. However, if ϵ is large (e.g., due to dust settling) then the reduced temperature $\tilde{T} = T(1 - f_d)$ may be lowered to enable instability.

As noted in Section 3.1, dust settling causes $\tilde{T}$ to *increase* away from the midplane. This contrasts with previous studies of GI in vertically stratified disks where the temperature decreases from the midplane (e.g., Mamatsashvili & Rice 2010; Kim et al. 2012; Lin 2014). While we expect that only the total surface density and characteristic temperatures are relevant to stability (Toomre 1964), a non-trivial vertical temperature structure, induced by dust, may modify the vertical structure of 3D waves and unstable modes.

Another potential connection to previous results for gas disks is gravito-turbulence. Cooling, self-gravitating gaseous disks sustain a turbulent state where shock heating due to gravitational instabilities is balanced by radiative cooling (Gammie 2001). Since dust–gas drift appears as a diffusion or cooling in our framework (Equation (15)), it may be conceivable to have "dusty gravito-turbulence." As self-gravity increases the local density, the associated pressure maxima attract dust particles, but the back-reaction onto the gas may try to flatten the pressure bump (Taki et al. 2016), thus enabling a quasi-steady state.

7.3.2. Rossby Wave Instability (RWI)

The RWI is a non-axisymmetric, 2D shear instability that operates in thin disks when it has radial structure (Lovelace

et al. 1999; Li et al. 2000). These studies consider adiabatic pure gas and show that instability is possible if there is an extremum in the generalized potential vorticity $\mathcal{V}_g = \kappa^2 \mathcal{S}_g^{-2/\gamma}/2\Omega_g \Sigma_g$, where $\mathcal{S}_g = P/\Sigma_g^\gamma$ is essentially the gas entropy. Here P should be interpreted as the vertically integrated pressure. The nonlinear result of the RWI is vortex formation (Li et al. 2001).

The dusty/adiabatic gas analogy implies that the condition for RWI in a polytropic dusty gas disk is an extremum,

$$\mathcal{V} = \frac{\kappa^2}{2\Omega\Sigma} \frac{1}{K^{2/\Gamma}} \left(1 + \frac{\Sigma_d}{\Sigma_g}\right)^2. \tag{66}$$

Thus RWI may also be triggered by extrema in the dust-to-gas ratio, e.g., narrow dust rings/gaps. This may lead to direct formation of dusty vortices, as opposed to dust-trapping by a pre-existing gas vortex (Barge & Sommeria 1995; Lyra & Lin 2013).

7.3.3. Convective Overstability (ConO)

The "ConO" was discovered in non-adiabatic, unstratified disk models of pure gas where the radial buoyancy frequency is such that $N_r^2 \equiv F_r \partial_r S/C_P < 0$ and cooling times $t_{cool} \sim \Omega_K^{-1}$. This combination leads to growing epicycles (Klahr & Hubbard 2014; Lyra 2014; Latter 2016).

Now consider a strictly isothermal dusty disk where the relevant entropy is dust-induced, $S_{eff} = -\ln(1 + \rho_d/\rho_g)$. Since $F_r \propto -\partial_r P > 0$ in typical disk models, ConO would require $\partial_r S_{eff} < 0$, implying that the dust-to-gas ratio increases *outward*. This might occur at special radial locations in protoplanetary disks, such as planet gaps. Dust-settling itself may also cause the midplane dust-to-gas ratio to increase outward (Takeuchi & Lin 2002).

Isothermal disks have $t_{cool} = 0$, so the pure gas ConO cannot exist. However, we have shown that dust–gas drag provides an effective energy source/sink to the mixture (Section 3.2). It would be interesting to explore whether or not dust–gas drag can play the role of cooling to enable a "dusty convective overstability."

7.3.4. Zombie Vortices

The "zombie vortex instability" (ZVI) is a non-axisymmetric, nonlinear instability discovered in pure gas disks (Marcus et al. 2015; Umurhan et al. 2016b). It operates by having finite-amplitude perturbations exciting "critical layers," where the intrinsic wave frequency of the perturbation matches the local vertical buoyancy frequency (Marcus et al. 2013). These critical layers roll up into vortices, exciting further critical layers. The process repeats itself and the result is an array of vortices.

Since the necessary physical ingredient for the ZVI is vertical buoyancy, it requires an almost purely adiabatic gas with long cooling times ($t_{cool}\Omega_K \gg 1$). This limits its applicability in typical protoplanetary disks to $\lesssim 1$ au (Lesur & Latter 2016; Malygin et al. 2017). However, this consideration assumes a dust-free disk as far as the dynamics is concerned.

On the other hand, we have shown that dust-loading induces an effective buoyancy even in isothermal disks. It is thus natural to ask whether or not the required adiabatic conditions for ZVI can be realized through dust-loading (specifically a

vertical gradient in the dust-to-gas ratio) and thus produce "dusty ZVI." This may allow the zombie vortices to develop $\gtrsim 1\,\mathrm{au}$ in PPDs.

7.4. Implications for Numerical Simulations

The one-fluid model with the terminal velocity approximation, Equations (5)–(7), has been applied to simulate dusty protoplanetary disks (Dipierro et al. 2015; Ragusa et al. 2017). These studies explicitly evolve the dust density.

However, the equivalence of dusty and adiabatic gas identified in this paper means that one need not implement a separate module for simulating the dust component in locally isothermal/polytropic gas. The standard energy equation substitutes for the dust continuity equation. Thus pure gas dynamic codes can be used to simulate protoplanetary dusty disks. When the sound speed c_s (or K) is not constant and/or the dust–gas coupling is imperfect, $t_s \neq 0$, one should add corresponding source terms in the energy equation (e.g., Equation (64)). The source term associated with dust–gas drag, $\mathcal{C}$, is analogous to radiative diffusion (Price & Laibe 2015) or thermal conduction, which is also common in modern hydrodynamics codes.

We have taken advantage of the equivalence of dusty and adiabatic gas to convert the popular PLUTO[5] hydrodynamics code (Mignone et al. 2007) into a dusty gas dynamics code appropriate for simulating protoplanetary disks coupled to small dust. In fact, our code is unaware of the fact that it is modeling dusty gas. We will apply this modified code—dPLUTO—to study dusty disk–planet interaction (J.-W. Chen & M.-K. Lin, in preparation). Preliminary results show that our approach reproduces features such as dusty rings associated with planet-induced gaps similar to those obtained from explicit two-fluid simulations (e.g., Dong et al. 2017).

8. Summary

In this paper, we examine the conditions under which the presence of dust can trigger instabilities in gaseous protoplanetary disks. To this end, we develop an analogy between isothermal dusty gas and pure ideal gas. The correspondence arises because drag forces reduce the relative velocity between gas and dust. In the limit of perfect dust–gas coupling, with stopping time $t_s \to 0$, dust is entrained in the gas. Then the dust-to-gas ratio ρ_d/ρ_g is conserved following the flow. This property is analogous to entropy conservation following an adiabatic, pure gas.

For finite drag, $t_s \neq 0$, the dust content of a parcel of the dusty gas mixture is no longer conserved. The parcel can exchange dust particles with neighboring parcels. This is analogous to heat exchange between a parcel of pure gas and its surroundings.

We explicitly show that for a fixed equation of state for the gas, the evolutionary equation for ρ_d/ρ_g may be replaced by an effective energy equation. This leads to a natural definition of the effective entropy of isothermal dusty gas as

$$S_{\mathrm{eff}} = \ln\left(\frac{c_s^2 \rho_g}{\rho_g + \rho_d}\right),$$

which implies that a nonuniform dust-to-gas ratio induces buoyancy forces. The effect of finite dust–gas friction appears as an energy source term. This analogy with standard hydrodynamics with cooling/heating allows us to find dusty

analogs of gaseous instabilities, and to provide thermodynamical interpretations of dust-drag instabilities.

We obtain the equivalent Solberg–Hoiland criteria for the axisymmetric stability of strictly isothermal, perfectly coupled dusty gas. Applying these to typical protoplanetary disks, we find that the vertical shear associated with dust layers *cannot* lead to axisymmetric instabilities, however thin the dust layer is. Instead, sharp radial edges in the dust-to-gas ratio could destabilize the disk, because these imply sharp gradients in the disk's effective entropy profile. Alternatively, if the dust is vertically well-mixed, then any radial gradient in ρ_d/ρ_g can destabilize the disk.

We apply our thermodynamic framework to interpret the Streaming Instability (SI; Youdin & Goodman 2005; Jacquet et al. 2011) and to generalize the gaseous Vertical Shear Instability (VSI; Nelson et al. 2013; Lin & Youdin 2015) to dusty disks. We explicitly show that in SI the evolution of gas pressure lags behind dust density. In fact, this is a general property of overstabilities driven by dust–gas drag. It takes a finite time for the gas to respond to the dust motion. A lag implies that there exists a time interval where the gas pressure of a parcel of the dusty gas mixture is increasing while dust is already being expelled. The dusty gas then does positive work that amplifies oscillations. This interpretation is analogous to stellar pulsational instabilities (Cox 1967).

For the VSI we find that dust-loading is generally stabilizing. In our disk models dust-loading does not affect VSI growth rates significantly, but meridional motions may be suppressed where the dust-induced vertical buoyancy dominates over vertical shear, consistent with our previous study (Lin & Youdin 2015). Since the dust-induced buoyancy forces increase away from the midplane, we find that dust-loading can stabilize "surface modes" of the VSI that would otherwise have the largest growth rates. We also show that radial variations in ρ_d/ρ_g can trigger a type of VSI, even when the usual sources of vertical shear—vertical dust gradients and radial temperature gradients—are negligible.

In a realistic disk, dust particles settle on a timescale $t_{\mathrm{settle}} \sim 1/t_s \Omega_K^2$ (Takeuchi & Lin 2002), compared with typical VSI growth timescales, $t_{\mathrm{grow}} \sim 1/h_g \Omega_K$. This suggest that particles with $t_s \Omega_K \lesssim h_g$ cannot settle against the VSI. On the other hand, larger particles with $t_s \Omega_K \gtrsim h_g$ should settle to form a dusty midplane. In fact, our calculations suggest that settling would stabilize the disk against VSI and allow further settling. The result may be a quiet, dusty midplane (unless non-axisymmetric instabilities develop, Chiang 2008) with VSI-turbulent gaseous atmospheres.

We also discuss future applications of our thermodynamic framework to study dusty protoplanetary disks. Because isothermal dusty gas has an effective entropy, we suggest that purely hydrodynamic processes, such as the Rossby Wave Instability (Li et al. 2000) or the Zombie Vortex Instability (Marcus et al. 2015), where entropy plays a role, could have dusty counterparts. Furthermore, hydrodynamic instabilities driven by thermal cooling, such as VSI in stably stratified disks (Lin & Youdin 2015) or the "Convective Overstability" (Klahr & Hubbard 2014; Lyra 2014), may also find dusty analogs because finite dust–gas drag is equivalent to a heat sink/source.

The dusty/adiabatic gas equivalence also offers a simple way to simulate dusty protoplanetary disks using purely hydrodynamic codes. All that is required is a re-interpretation of the fluid variables and additional source terms in the usual energy equation. The latter is already available in many public

---

[5] http://plutocode.ph.unito.it/

codes. In a follow-up work we will apply this approach to study dusty disk–planet interaction.

Appendix A
Variational Principle

Here we consider the more general equation of state for the gas with $P = K\rho_g^\Gamma$ where K is a prescribed function of position and Γ is a constant. The effective energy equation is then Equation (64), which generalizes Equation (15). Assuming axisymmetry throughout, we linearize this equation along with Equations (5), (7), and (11) to give

$$i\sigma\frac{\Delta\rho}{\rho} = i\sigma\frac{\delta\rho}{\rho} - \delta\boldsymbol{v}\cdot\nabla\ln\rho = \nabla\cdot\delta\boldsymbol{v}, \tag{67}$$

$$i\sigma\frac{\Delta P}{P} = i\sigma\frac{\delta P}{P} - \delta\boldsymbol{v}\cdot\nabla\ln P$$
$$= \Gamma\nabla\cdot\delta\boldsymbol{v} - \delta\boldsymbol{v}\cdot\nabla\ln K - \frac{\delta\mathcal{C}}{P}, \tag{68}$$

$$-i\sigma\delta v_r = 2\Omega\delta v_\phi + \hat{\boldsymbol{r}}\cdot\delta\boldsymbol{F} - \hat{\boldsymbol{r}}\cdot\nabla\delta\psi, \tag{69}$$

$$i\sigma\delta v_\phi = \frac{\kappa^2}{2\Omega}\delta v_r + \frac{\partial v_\phi}{\partial z}\delta v_z, \tag{70}$$

$$-i\sigma\delta v_z = \hat{\boldsymbol{z}}\cdot\delta\boldsymbol{F} - \hat{\boldsymbol{z}}\cdot\nabla\delta\psi, \tag{71}$$

$$\nabla^2\delta\psi = 4\pi G\delta\rho. \tag{72}$$

where the linearized pressure force $\delta\boldsymbol{F}$ is given in Appendix B. Recall that $\Delta = \delta + \boldsymbol{\xi}\cdot\nabla$ is the Lagrangian perturbation and $\boldsymbol{\xi}$ is the Lagrangian displacement. In addition, $i\sigma\boldsymbol{\xi}\cdot\nabla = -\delta\boldsymbol{v}\cdot\nabla$ for axisymmetric flow. These equations do not assume the radially local approximation used in numerical computations. Note that Equations (67)–(68) imply

$$|\sigma|^2\frac{\Delta P}{P}\frac{\Delta\rho^*}{\rho} = \Gamma\,|\nabla\cdot\delta\boldsymbol{v}|^2 - \nabla\cdot\delta\boldsymbol{v}^*\left(\delta\boldsymbol{v}\cdot\nabla\ln K + \frac{\delta\mathcal{C}}{P}\right), \tag{73}$$

so the first (real) term on the right does not contribute to $\mathrm{Im}\,(\Delta P\Delta\rho^*)$. Setting K to constant and taking the imaginary part gives Equation (35).

From the linearized meridional momentum equations, we find

$$\sigma^2\int\rho(|\delta v_r|^2 + |\delta v_z|^2)dV = \int\left(\rho\kappa^2|\delta v_r|^2 + \rho r\frac{\partial\Omega^2}{\partial z}\delta v_z\delta v_r^*\right.$$
$$\left. + i\sigma\rho\delta\boldsymbol{F}\cdot\delta\boldsymbol{v}^* - i\sigma\rho\nabla\delta\psi\cdot\delta\boldsymbol{v}^*\right)dV, \tag{74}$$

where the integral is taken over the volume of the fluid. Integrating by parts and ignoring surface integrals, the last term is

$$\int i\sigma\rho\delta\boldsymbol{F}\cdot\delta\boldsymbol{v}^*dV$$

$$= \int\left(i\sigma\frac{\delta\rho}{\rho}\delta\boldsymbol{v}^*\cdot\nabla P - i\sigma\delta\boldsymbol{v}^*\cdot\nabla\delta P\right)dV$$

$$= \int\left(i\sigma\frac{\delta\rho}{\rho}\delta\boldsymbol{v}^*\cdot\nabla P + i\sigma\delta P\nabla\cdot\delta\boldsymbol{v}^*\right)dV$$

$$= \int\left[\left(i\sigma\frac{\delta P}{\Gamma P} - \delta\boldsymbol{v}\cdot\nabla S_{\text{eff}} + \frac{\delta\boldsymbol{v}}{\Gamma}\cdot\nabla\ln K + \frac{\delta\mathcal{C}}{\Gamma P}\right)\right.$$
$$\left.\times\delta\boldsymbol{v}^*\cdot\nabla P + i\sigma\delta P\nabla\cdot\delta\boldsymbol{v}^*\right]dV$$

$$= \int\left[i\sigma\frac{\delta P}{\Gamma P}(\delta\boldsymbol{v}^*\cdot\nabla P + \Gamma P\nabla\cdot\delta\boldsymbol{v}^*) + (\delta\boldsymbol{v}^*\cdot\nabla P)\right.$$
$$\left.\times\left(\frac{\delta\boldsymbol{v}}{\Gamma}\cdot\nabla\ln K + \frac{\delta\mathcal{C}}{\Gamma P} - \delta\boldsymbol{v}\cdot\nabla S_{\text{eff}}\right)\right]dV$$

$$= \int\left\{\left[\nabla\cdot\delta\boldsymbol{v} + \frac{\delta\boldsymbol{v}}{\Gamma}\cdot\nabla\ln P - \frac{\delta\boldsymbol{v}}{\Gamma}\cdot\nabla\ln K - \frac{\delta\mathcal{C}}{\Gamma P}\right]\right.$$
$$\times(\delta\boldsymbol{v}^*\cdot\nabla P + \Gamma P\nabla\cdot\delta\boldsymbol{v}^*)$$
$$\left. + (\delta\boldsymbol{v}^*\cdot\nabla P)\left(\frac{\delta\boldsymbol{v}}{\Gamma}\cdot\nabla\ln K + \frac{\delta\mathcal{C}}{\Gamma P} - \delta\boldsymbol{v}\cdot\nabla S_{\text{eff}}\right)\right\}dV$$

$$= \int\left[\frac{1}{\Gamma P}\,|\delta\boldsymbol{v}\cdot\nabla P + \Gamma P\nabla\cdot\delta\boldsymbol{v}|^2 - (\delta\boldsymbol{v}^*\cdot\nabla P)\right.$$
$$\left.\times(\delta\boldsymbol{v}\cdot\nabla S_{\text{eff}}) - P(\nabla\cdot\delta\boldsymbol{v}^*)\left(\delta\boldsymbol{v}\cdot\nabla\ln K + \frac{\delta\mathcal{C}}{P}\right)\right]dV, \tag{75}$$

where $S_{\text{eff}} \equiv \ln(P^{1/\Gamma}/\rho)$. The self-gravitational part of Equation (74) is, again neglecting surface terms when integrating by parts,

$$-\int i\sigma\rho\nabla\delta\psi\cdot\delta\boldsymbol{v}^* = \int i\sigma\delta\psi\nabla\cdot(\rho\delta\boldsymbol{v}^*)\,dV$$
$$= \int|\sigma|^2\delta\psi\delta\rho^*dV = -\frac{1}{4\pi G}\int|\sigma|^2|\nabla\psi|^2dV, \tag{76}$$

where the linearized continuity and Poisson equations have been used.

Hence,

$$\sigma^2\int\rho(|\delta v_r|^2 + |\delta v_z|^2)dV$$

$$= \int\left\{\rho|\delta v_r|^2\left(\kappa^2 - \frac{1}{\rho}\frac{\partial P}{\partial r}\frac{\partial S_{\text{eff}}}{\partial r}\right) + \rho|\delta v_z|^2\left(-\frac{1}{\rho}\frac{\partial P}{\partial z}\frac{\partial S_{\text{eff}}}{\partial z}\right)\right.$$

$$+ \rho\delta v_z\delta v_r^*\left(r\frac{\partial\Omega^2}{\partial z} - \frac{1}{\rho}\frac{\partial P}{\partial r}\frac{\partial S_{\text{eff}}}{\partial z}\right)$$

$$+ \rho\delta v_z^*\delta v_r\left(-\frac{1}{\rho}\frac{\partial P}{\partial z}\frac{\partial S_{\text{eff}}}{\partial r}\right)$$

$$\left. + \frac{1}{\Gamma P}\,|\delta\boldsymbol{v}\cdot\nabla P + \Gamma P\nabla\cdot\delta\boldsymbol{v}|^2 - \frac{1}{4\pi G}\,|\sigma\nabla\delta\psi|^2\right\}dV$$

$$- \int P(\nabla\cdot\delta\boldsymbol{v}^*)(\delta\boldsymbol{v}\cdot\nabla\ln K)dV$$

$$- \int(\nabla\cdot\delta\boldsymbol{v}^*)\delta\mathcal{C}dV. \tag{77}$$

Note that the coefficients of $\delta v_z \delta v_r^*$ and $\delta v_z^* \delta v_r$ are equal owing to the equilibrium state (Equation (23)). The non-self-gravitating case with $\Gamma = 1$, $K = c_s^2$ gives Equation (26). Similar integral relations are given by Kato (1978), Kley et al. (1993), and Latter & Ogilvie (2006).

Appendix B
Linearized Pressure Forces and Their Divergence

The linearized form of the pressure force $\boldsymbol{F} = -\nabla P / \rho$ is

$$\delta \boldsymbol{F} = -\frac{\delta \rho}{\rho} \boldsymbol{F} - \frac{1}{\rho} \nabla \delta P, \tag{78}$$

with divergence

$$\nabla \cdot \delta \boldsymbol{F} = -\nabla \left(\frac{\delta \rho}{\rho} \right) \cdot \boldsymbol{F}$$
$$- \frac{\delta \rho}{\rho} \nabla \cdot \boldsymbol{F} + \nabla \ln \rho \cdot \frac{\nabla \delta P}{\rho} - \frac{1}{\rho} \nabla^2 \delta P. \tag{79}$$

The explicit forms for $\delta \boldsymbol{F}$ and $\nabla \cdot \delta \boldsymbol{F}$, in the radially local approximation, are

$$\delta F_r = -W F_r - i k_x Q, \tag{80}$$

$$\delta F_z = -W F_z - [Q' + Q(\ln \rho)'] = -i\sigma \delta v_z + \delta \psi', \tag{81}$$

where the last equality is the linearized vertical momentum equation, and

$$\nabla \cdot \delta \boldsymbol{F} = F_r (\partial_r \ln \rho - i k_x) W - F_z W'$$
$$- W \nabla \cdot \boldsymbol{F} + i k_x Q \partial_r \ln \rho + (\ln \rho)' [Q' + Q(\ln \rho)']$$
$$+ k_x^2 Q - \{ Q'' + 2Q'(\ln \rho)'$$
$$+ Q[(\ln \rho)'' + (\ln \rho)'^2] \}$$
$$= [(\partial_r \ln \rho - i k_x) F_r - \nabla \cdot \boldsymbol{F} + F_z'] W$$
$$+ (i k_x \partial_r \ln \rho + k_x^2) Q - i\sigma \delta v_z' + \delta \psi''. \tag{82}$$

Appendix C
Linearized Dust Diffusion

We consider small grains in the Epstein regime, with fixed internal density and size, so that

$$t_s = \frac{\mathcal{K}}{\rho c_s} \tag{83}$$

(Price & Laibe 2015), where $\mathcal{K}$ is a constant. Then the dust diffusion function becomes

$$\mathcal{C} \equiv c_s^2 \nabla \cdot (f_d t_s \nabla P) = -\mathcal{K} c_s^2 \nabla \cdot \left(\frac{f_d}{c_s} \boldsymbol{F} \right)$$
$$= -\mathcal{K} c_s \left(\boldsymbol{F} \cdot \nabla f_d + f_d \nabla \cdot \boldsymbol{F} - \frac{1}{2} f_d \boldsymbol{F} \cdot \nabla \ln c_s^2 \right). \tag{84}$$

Linearizing,

$$-\frac{\delta \mathcal{C}}{\mathcal{K} c_s} = \boldsymbol{F} \cdot \nabla \delta f_d + \delta \boldsymbol{F} \cdot \nabla f_d + \delta f_d \nabla \cdot \boldsymbol{F}$$
$$+ f_d \nabla \cdot \delta \boldsymbol{F} - \frac{1}{2} \nabla \ln c_s^2 \cdot (\boldsymbol{F} \delta f_d + f_d \delta \boldsymbol{F}). \tag{85}$$

The linearized dust fraction δf_d and its derivatives in the radially local approximation are given by

$$\delta f_d = (1 - f_d) W - \frac{Q}{c_s^2}, \tag{86}$$

$$\partial_r \delta f_d = [(1 - f_d)(i k_x - \partial_r \ln \rho) - \partial_r f_d] W$$
$$+ (\partial_r \ln c_s^2 + \partial_r \ln \rho - i k_x) \frac{Q}{c_s^2}, \tag{87}$$

$$\delta f_d' = (1 - f_d) W' - f_d' W - \left(\frac{Q}{c_s^2} \right)'. \tag{88}$$

Appendix D
One-fluid Dispersion Relation for the Streaming Instability

We consider an unstratified disk with $\Phi = \Phi(r)$ (by setting $z = 0$ in Equation (10)) so that $\partial_z P = \partial_z \rho = 0$. The background $\partial_r P / \rho$, f_d are constant input parameters. We Fourier analyze in r and z so that $\partial_z \to i k_z$ and $\partial_r \to i k_x$ when acting on perturbations, and denote $|\boldsymbol{k}|^2 \equiv k_x^2 + k_z^2$. We consider large k_x and thus neglect background gradients when compared to that of perturbations. This is also done in most local studies of dusty disks (e.g., Youdin & Johansen 2007). The linearized equations, after eliminating the azimuthal velocity, are

$$i\sigma W = \nabla \cdot \delta \boldsymbol{v} = i k_x \delta v_x + i k_z \delta v_z, \tag{89}$$

$$\sigma^2 \delta v_x = \kappa^2 \delta v_x - i\sigma F_r W + k_x \sigma Q, \tag{90}$$

$$-i\sigma \delta v_z = -i k_z Q, \tag{91}$$

$$i\zeta \sigma Q = \frac{P}{\rho} \nabla \cdot \delta \boldsymbol{v} - \frac{\delta \mathcal{C}}{\rho}. \tag{92}$$

The artificial factor $\zeta = 1$ is inserted to keep track of the left of the energy equation. Setting ζ to zero is equivalent to assuming incompressible gas (Jacquet et al. 2011). The linearized dust diffusion function (Appendix C), under the above approximations, is

$$-\frac{\delta \mathcal{C}}{\rho} = t_s c_s^2 [i k_x F_r (1 - 2f_d) W + f_d |\boldsymbol{k}|^2 Q]. \tag{93}$$

We eliminate the velocity perturbations to obtain

$$(i\zeta \sigma - t_s c_s^2 f_d |\boldsymbol{k}|^2) Q = i \left[\frac{P}{\rho} \sigma + k_x t_s c_s^2 F_r (1 - 2f_d) \right] W, \tag{94}$$

$$\sigma^2 (\kappa^2 - \sigma^2 - i k_x F_r) W = (k_z^2 \kappa^2 - \sigma^2 |\boldsymbol{k}|^2) Q, \tag{95}$$

which yields the dispersion relation

$$\frac{\zeta}{c_s^2 |\boldsymbol{k}|^2} \sigma^5 + i f_d t_s \sigma^4 - \left[\frac{\zeta}{c_s^2 |\boldsymbol{k}|^2} (\kappa^2 - i k_x F_r) + (1 - f_d) \right] \sigma^3$$
$$- i t_s [f_d \kappa^2 - i k_x F_r (1 - f_d)] \sigma^2$$
$$+ (1 - f_d) \left(\frac{k_z \kappa}{|\boldsymbol{k}|} \right)^2 \sigma + k_x t_s F_r (1 - 2f_d) \left(\frac{k_z \kappa}{|\boldsymbol{k}|} \right)^2 = 0. \tag{96}$$

The equation of state $P = c_s^2 (1 - f_d) \rho$ was used.

D.1. Incompressible Gas Limit

We can set $\zeta = 0$ or consider $c_s^2 \to \infty$ to obtain the incompressible gas limit. Using $\tau_s \equiv t_s/(1 - f_d)$, we obtain

$$if_d \tau_s \sigma^4 - \sigma^3 - \tau_s[if_d \kappa^2 + k_x F_r(1 - f_d)]\sigma^2$$
$$+ \left(\frac{k_z \kappa}{|\boldsymbol{k}|}\right)^2 \sigma + k_x \tau_s F_r(1 - 2f_d)\left(\frac{k_z \kappa}{|\boldsymbol{k}|}\right)^2 = 0, \qquad (97)$$

as derived by Jacquet et al. (2011) and Laibe & Price (2014) for the SI. If $|\sigma|/\Omega_K = O(\tau_s \Omega_K)$ and $\tau_s \Omega_K \ll 1$, then the quartic term is small and may be neglected. In that case we obtain the cubic dispersion relation of Youdin & Goodman (2005).

D.2. Approximate Solutions in the Dust-rich Limit

Here we seek analytic solutions for the SI by examining limiting cases and with additional approximations. We will fix k_z, f_d and maximize growth rates over k_x. It turns out that simple solutions exist in the dust-rich case with f_d near unity. We consider small stopping times, $\tau_s \to 0$, and assume that the corresponding optimum $k_x \to \infty$.

We begin with the incompressible dispersion relation, Equation (97). We assume a Keplerian disk ($\Omega = \kappa = \Omega_K$), and low-frequency modes ($|\sigma| \ll \Omega_K$), which allows us to neglect the quartic term. (This is also necessary to avoid spurious modes, see Appendix D.3.) In dimensionless form, the dispersion relation is

$$\nu^3 + St[if_d + 2K_x f_g(1 - f_d)]\nu^2 - \left(\frac{K_z}{K_x}\right)^2 \nu$$
$$- 2St K_x f_g(1 - 2f_d)\left(\frac{K_z}{K_x}\right)^2 = 0, \qquad (98)$$

where $\nu = \sigma/\Omega_K$, $St = \tau_s \Omega_K$, $f_g = 1 - f_d$ (the gas fraction), and recall that $K_{x,z} = \eta r k_{x,z}$. We have used $F_r = 2\eta f_g r \Omega^2$ and considered large K_x.

Analytic expressions for cubic roots are unwieldy. To keep the problem tractable, let us *assume* at this stage that the quadratic term can be neglected compared to the last term. That is,

$$\left| \frac{if_d}{2K_x f_g} + (1 - f_d) \right| |K_x \nu|^2 \ll K_z^2(2f_d - 1). \qquad (99)$$

(The imaginary term can be neglected for fixed f_d but allowing $K_x \to \infty$.) We show in Appendix D.2.2 that this simplification is valid for dust-rich disks.

Equation (98) now becomes the depressed cubic

$$\nu^3 - \mathcal{P}\nu = \mathcal{Q}, \qquad (100)$$

where $\mathcal{P}$ and $\mathcal{Q}$ can be read off Equation (98). This can be solved with Vieta's substitution

$$\nu = \mu + \frac{\mathcal{P}}{3\mu}, \qquad (101)$$

then Equation (100) becomes a quadratic for μ^3,

$$\mu^6 - \mathcal{Q}\mu^3 + \frac{\mathcal{P}^3}{27} = 0. \qquad (102)$$

The solution is

$$\mu^3 = \frac{\mathcal{Q}}{2}\left(1 \pm \sqrt{1 - \frac{4\mathcal{P}^3}{27\mathcal{Q}^2}}\right)$$
$$= St f_g(1 - 2f_d)\frac{K_z^2}{K_x}$$
$$\times \left\{1 \pm \sqrt{1 - \frac{K_z^2}{27K_x^2[St K_x f_g(1 - 2f_d)]^2}}\right\}. \qquad (103)$$

At this point we assume that the term $\propto K_z^2$ inside the square root may be neglected. That is,

$$K_z^2 \ll 27(K_x^2 St)^2[f_g(1 - 2f_d)]^2. \qquad (104)$$

We show in Appendix D.2.2 that this is readily satisfied. Then $\mu \simeq \mathcal{Q}^{1/3}$.

Now, remembering that we are considering the dust-rich limit with $1 - 2f_d < 0$, the explicit solution for μ is

$$\mu = \left[2St f_g(2f_d - 1)\frac{K_z^2}{K_x}\right]^{1/3} e^{i\pi/3}. \qquad (105)$$

We have chosen the complex root for instability. Inserting this into Equation (101) gives the eigenfrequency ν:

$$Re(\nu) = \frac{1}{2}(\mathcal{A}St^{1/3}K_x^{-1/3} + \mathcal{B}St^{-1/3}K_x^{-5/3}), \qquad (106)$$

$$Im(\nu) = \frac{\sqrt{3}}{2}(\mathcal{A}St^{1/3}K_x^{-1/3} - \mathcal{B}St^{-1/3}K_x^{-5/3}), \qquad (107)$$

where

$$\mathcal{A} = [2f_g(2f_d - 1)K_z^2]^{1/3}, \qquad (108)$$

$$\mathcal{B} = \frac{K_z^2}{3\mathcal{A}}. \qquad (109)$$

Maximizing growth rates over K_x by setting $\partial Im(\nu)/\partial K_x = 0$, we find the optimum wavenumber is given by

$$K_x = \left(\frac{5\mathcal{B}}{\mathcal{A}}\right)^{3/4} St^{-1/2} = \left(\frac{5}{3}\right)^{3/4} \sqrt{\frac{K_z}{2f_g(2f_d - 1)St}}. \qquad (110)$$

The maximum growth rate is then

$$max[Im(\nu)] = \frac{2\sqrt{3}}{5^{5/4}}\frac{\mathcal{A}^{5/4}}{\mathcal{B}^{1/4}}\sqrt{St}$$
$$= \frac{2\sqrt{2} \times 3^{3/4}}{5^{5/4}}\sqrt{f_g(2f_d - 1)K_z St}. \qquad (111)$$

and the real frequency $Re(\nu) = (\sqrt{3}/2)Im(\nu)$. We see that as $\tau_s \to 0$, the most unstable radial wavenumber diverges, $K_x \propto \tau_s^{-1/2} \to \infty$ with a vanishing growth rate, $max(s) \propto \sqrt{\tau_s} \to 0$. This corresponds to instability at arbitrarily small radial length scales.

D.2.1. Finite Phase Lag as $\tau_s \to 0$

An interesting property of the special solutions described above is that there is always a phase lag between the Lagrangian pressure and density perturbations. Since $Re(\nu) > 0$, the phase lag may be defined as $\varphi = \arg(\Delta P \Delta \rho^*)$. (Note that we may set $\Delta \rho = 1$ without loss of generality.) It may be shown that $\Delta P \simeq i\delta v_x \partial_r P/\sigma$ in the limit of large K_x. To obtain δv_x we use

Equation (90) in the low-frequency limit. The expression for δv_x involves the Eulerian pressure perturbation, δP, for which we use Equation (94) and assume incompressibility ($\zeta \to 0$).

With these additional simplifications the phase lag φ is given via

$$\tan \varphi = \frac{\mathrm{Im}(\Delta P \Delta \rho^*)}{\mathrm{Re}(\Delta P \Delta \rho^*)} \simeq \frac{K_x \,\mathrm{Im}(\nu)}{2 f_g^2 \mathrm{St} K_x^2 + K_x \mathrm{Re}(\nu)}. \quad (112)$$

From here it is clear for the above solutions, where $K_x \propto \mathrm{St}^{-1/2}$ and $\nu \propto \mathrm{St}^{1/2}$, that φ is a constant. Explicitly inserting the solutions gives

$$\tan \varphi = \frac{2 \times 3^{3/2}(2 f_d - 1)}{16 - 7 f_d}. \quad (113)$$

For the case shown in Figure 4 with $f_d = 0.75$, we have $\varphi \simeq 26°$, comparable to the $\sim 30°$ obtained from numerical solutions.

D.2.2. Consistency Check

Here we check if the above explicit solutions are consistent with the assumptions used to obtain them. Inserting the solutions for the most unstable mode, we find Equation (99) becomes

$$f_d \gg \frac{12}{17} \simeq 0.7. \quad (114)$$

Since $f_d \leqslant 1$, this requirement can only be marginally satisfied. However, we find that this mostly gives errors in the real frequency (see Figure 4), while growth rates are still captured correctly. On the other hand, the assumption of Equation (104) becomes the trivial inequality

$$1 \ll \frac{27}{4}\left(\frac{5}{3}\right)^3 \simeq 30, \quad (115)$$

so Equation (104) is satisfied, which justifies the approximate solution for μ in Equation (105).

Ultimately, the validity of these assumptions is justified a posteriori by comparison with the solution to the full equations in Figure 4.

D.3. Spuriously Growing Epicycles

A caveat of the dispersion relations Equations (96) and (97) is that they admit spurious unstable modes with $|\sigma| \gtrsim \Omega$. This violates the one-fluid approximation to model dusty gas. We demonstrate this below by considering the incompressible dispersion relation. (We checked numerically that compressibility has negligible effects on the modes examined.)

Consider the limit $k_z = 0$. Then Equation (97) becomes

$$i\nu^2 - \frac{\nu}{f_d \mathrm{St}} - \left[i + 2 K_x \frac{f_g}{f_d}(1 - f_d)\right] = 0 \quad (116)$$

in dimensionless form. Neglecting the quadratic term leads to stability, $\mathrm{Im}(\nu) < 0$. This is consistent with a full two-fluid analysis (Youdin & Goodman 2005).

However, solving Equation (116) explicitly assuming $|f_d \tau_s \mathrm{Im}(\nu)| \ll 1$ would yield

$$\mathrm{Re}(\nu) \simeq 2 K_x (1 - f_d)^2 \mathrm{St} \sim O(1) \quad (117)$$

$$\mathrm{Im}(\nu) \simeq f_d \mathrm{St}[4 K_x^2 (1 - f_d)^4 \mathrm{St}^2 - 1]. \quad (118)$$
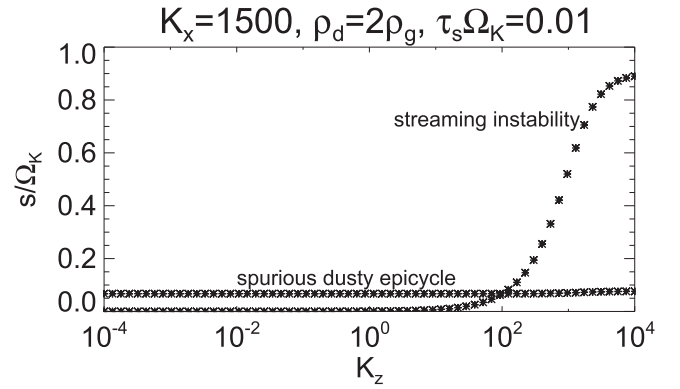

Figure 16. Growth rates of dust-drag instabilities with fixed radial wavenumber and dust-to-gas ratio, as a function of the vertical wavenumber at fixed stopping time.

Accordingly, growth is possible if

$$\mathrm{St} > \frac{1}{2 K_x (1 - f_d)^2}. \quad (119)$$

Alternatively, for fixed τ_s growth is enabled by a sufficiently large K_x. Unlike the SI, which is strongly suppressed when $f_d = 1/2$, these modes can still grow at equal dust-to-gas ratio.

These growing epicycles with $|\omega| \gtrsim \kappa$ are absent from full two-fluid models (Youdin & Goodman 2005). The discrepancy lies in the fact that the one-fluid equations, to first order in τ_s, are only valid for low-frequency waves with $|\sigma| \lesssim \Omega$. Thus only low-frequency modes should be retained from analyses based on Equations (5)–(8).

Figure 16 shows unstable modes found from Equation (96) as a function of K_z at fixed $K_x = 1500$, $\epsilon = 2$, and $\tau_s \Omega_K = 0.01$. The growth rates of the (spurious) overstable dusty epicycles are weakly dependent on K_z and are well approximated by that in the limit $K_z = 0$, Equation (118). For the case considered in Figure 16 we find $s \simeq 0.067 \Omega_K$, as observed. By contrast, the SI requires $K_z > 0$, and it dominates when $K_z \gtrsim 100$.

Care must be taken if the first-order one-fluid equations are used to simulate dusty gas. For example, 2D, razor-thin disks would allow the spurious epicycles to dominate, since in that case the SI cannot operate. However, Figure 16 shows that the SI should dominate in realistic 3D disks where a range of K_z is allowed.

Thus simulations based on the first-order one-fluid equations should be set up to suppress these spurious epicycles. This might be achieved, for example, through physical or numerical viscosity to eliminate high-k_x modes, since for fixed disk/dust parameters these spurious epicycles operate only at sufficiently small radial wavelengths. Alternatively, one needs to ensure that the physical instabilities of interest have larger growth rates than the spurious epicycles.

References

Ayliffe, B. A., Laibe, G., Price, D. J., & Bate, M. R. 2012, MNRAS, 423, 1450
Bai, X.-N., & Stone, J. M. 2010a, ApJ, 722, 1437
Bai, X.-N., & Stone, J. M. 2010b, ApJS, 190, 297
Barge, P., & Sommeria, J. 1995, A&A, 295, L1
Barker, A. J., & Latter, H. N. 2015, MNRAS, 450, 21
Barranco, J. A. 2009, ApJ, 691, 907
Barrière-Fouchet, L., Gonzalez, J.-F., Murray, J. R., Humble, R. J., & Maddison, S. T. 2005, A&A, 443, 185

Baruteau, C., & Zhu, Z. 2016, MNRAS, 458, 3927
Chiang, E. 2008, ApJ, 675, 1549
Chiang, E., & Youdin, A. N. 2010, AREPS, 38, 493
Chiang, E. I., & Goldreich, P. 1997, ApJ, 490, 368
Cox, J. P. 1967, in IAU Symp. 28, Aerodynamic Phenomena in Stellar
    Atmospheres, ed. R. N. Thomas (Cambridge: Cambridge Univ. Press), 3
Dipierro, G., Price, D., Laibe, G., et al. 2015, MNRAS, 453, L73
Dong, R., Li, S., Chiang, E., & Li, H. 2017, ApJ, 843, 127
Fu, W., Li, H., Lubow, S., Li, S., & Liang, E. 2014, ApJL, 795, L39
Gammie, C. F. 1996, ApJ, 457, 355
Gammie, C. F. 2001, ApJ, 553, 174
Gibbons, P. G., Mamatsashvili, G. R., & Rice, W. K. M. 2015, MNRAS,
    453, 4232
Goldreich, P., & Ward, W. R. 1973, ApJ, 183, 1051
Hopkins, P. F., & Squire, J. 2017, arXiv:1707.02997
Jacquet, E., Balbus, S., & Latter, H. 2011, MNRAS, 415, 3591
Johansen, A., Henning, T., & Klahr, H. 2006, ApJ, 643, 1219
Johansen, A., & Youdin, A. 2007, ApJ, 662, 627
Kato, S. 1978, MNRAS, 185, 629
Kim, J.-G., Kim, W.-T., Seo, Y. M., & Hong, S. S. 2012, ApJ, 761, 131
Klahr, H., & Hubbard, A. 2014, ApJ, 788, 21
Kley, W., Papaloizou, J. C. B., & Lin, D. N. C. 1993, ApJ, 409, 739
Kowalik, K., Hanasz, M., Wóltański, D., & Gawryszczak, A. 2013, MNRAS,
    434, 1460
Laibe, G., & Price, D. J. 2012, MNRAS, 420, 2345
Laibe, G., & Price, D. J. 2014, MNRAS, 440, 2136
Lambrechts, M., Johansen, A., Capelo, H. L., Blum, J., & Bodenschatz, E.
    2016, A&A, 591, A133
Latter, H. N. 2016, MNRAS, 455, 2608
Latter, H. N., & Ogilvie, G. I. 2006, MNRAS, 372, 1829
Latter, H. N., & Rosca, R. 2017, MNRAS, 464, 1923
Lee, A. T., Chiang, E., Asay-Davis, X., & Barranco, J. 2010, ApJ, 718, 1367
Lesur, G. R. J., & Latter, H. 2016, MNRAS, 462, 4549
Li, H., Colgate, S. A., Wendroff, B., & Liska, R. 2001, ApJ, 551, 874
Li, H., Finn, J. M., Lovelace, R. V. E., & Colgate, S. A. 2000, ApJ, 533, 1023
Lin, M.-K. 2014, ApJ, 790, 13
Lin, M.-K., & Kratter, K. M. 2016, ApJ, 824, 91
Lin, M.-K., & Youdin, A. N. 2015, ApJ, 811, 17
Lorén-Aguilar, P., & Bate, M. R. 2014, MNRAS, 443, 927
Lorén-Aguilar, P., & Bate, M. R. 2015, MNRAS, 453, L78
Lorén-Aguilar, P., & Bate, M. R. 2016, MNRAS, 457, L54
Lovelace, R. V. E., Li, H., Colgate, S. A., & Nelson, A. F. 1999, ApJ, 513, 805
Lyra, W. 2014, ApJ, 789, 77
Lyra, W., & Lin, M.-K. 2013, ApJ, 775, 17

Malygin, M. G., Klahr, H., Semenov, D., Henning, T., & Dullemond, C. P.
    2017, A&A, 605, A30
Mamatsashvili, G. R., & Rice, W. K. M. 2010, MNRAS, 406, 2050
Marcus, P. S., Pei, S., Jiang, C.-H., et al. 2015, ApJ, 808, 87
Marcus, P. S., Pei, S., Jiang, C.-H., & Hassanzadeh, P. 2013, PhRvL, 111,
    084501
Meheut, H., Meliani, Z., Varniere, P., & Benz, W. 2012, A&A, 545, A134
Michikoshi, S., Kokubo, E., & Inutsuka, S.-i. 2012, ApJ, 746, 35
Mignone, A., Bodo, G., Massaglia, S., et al. 2007, ApJS, 170, 228
Nelson, R. P., & Gressel, O. 2010, MNRAS, 409, 639
Nelson, R. P., Gressel, O., & Umurhan, O. M. 2013, MNRAS, 435, 2610
Ogilvie, G. I. 2016, JPlPh, 82, 205820301
Paardekooper, S.-J., & Mellema, G. 2006, A&A, 453, 1129
Price, D. J., & Laibe, G. 2015, MNRAS, 451, 813
Ragusa, E., Dipierro, G., Lodato, G., Laibe, G., & Price, D. J. 2017, MNRAS,
    464, 1449
Samadi, R., Belkacem, K., & Sonoi, T. 2015, in EAS Publications Ser. 73 (Les
    Ulis: EDP Sciences), 111
Shi, J.-M., & Chiang, E. 2013, ApJ, 764, 20
Simon, J. B., Armitage, P. J., Li, R., & Youdin, A. N. 2016, ApJ, 822, 55
Squire, J., & Hopkins, P. F. 2017, arXiv:1706.05020
Stamatellos, D., & Whitworth, A. P. 2008, A&A, 480, 879
Surville, C., Mayer, L., & Lin, D. N. C. 2016, ApJ, 831, 82
Takahashi, S. Z., & Inutsuka, S.-I. 2014, ApJ, 794, 55
Takahashi, S. Z., & Inutsuka, S.-I. 2016, AJ, 152, 184
Takeuchi, T., & Lin, D. N. C. 2002, ApJ, 581, 1344
Taki, T., Fujimoto, M., & Ida, S. 2016, A&A, 591, A86
Tassoul, J. 1978, Theory of Rotating Stars (Princeton, NJ: Princeton Univ.
    Press)
Thompson, C., & Stevenson, D. J. 1988, ApJ, 333, 452
Toomre, A. 1964, ApJ, 139, 1217
Umurhan, O. M., Nelson, R. P., & Gressel, O. 2016a, A&A, 586, A33
Umurhan, O. M., Shariff, K., & Cuzzi, J. N. 2016b, ApJ, 830, 95
Ward, W. R. 2000, in Origin of the Earth and Moon, ed. R. M. Canup,
    K. Righter et al. (Tucson, AZ: University of Arizona Press), 75
Weidenschilling, S. J. 1977, MNRAS, 180, 57
Yang, C.-C., & Johansen, A. 2014, ApJ, 792, 86
Yang, C.-C., & Johansen, A. 2016, ApJS, 224, 39
Youdin, A., & Johansen, A. 2007, ApJ, 662, 613
Youdin, A. N. 2011, ApJ, 731, 99
Youdin, A. N., & Goodman, J. 2005, ApJ, 620, 459
Youdin, A. N., & Shu, F. H. 2002, ApJ, 580, 494
Zhu, Z., Stone, J. M., Rafikov, R. R., & Bai, X.-n. 2014, ApJ, 785,
    122